Studying dawn-dusk asymmetries of Mercury's magnetotail using MHD-EPIC simulations

Yuxi Chen[1], Gábor Tóth [1], Xianzhe Jia[1], James A. Slavin[1], Weijie Sun[1], Stefano Markidis[2], Tamas I. Gombosi[1], Jim M. Raines[1]

[1]Department of Climate and Space Sciences and Engineering, University of Michigan, , Ann Arbor, MI, USA

[2]KTH, Stockholm, Sweden.

Key Points:

- Dawnside current sheet is thicker than the duskside
- Magnetic reconnection prefers dawnside under strong IMF driving
- Almost all dipolarization events, high-speed proton and electron planetward flows concentrate on the dawnside

Corresponding author: Yuxi Chen, yuxichen@umich.edu

Abstract

MESSENGER has observed a lot of dawn-dusk asymmetries in Mercury's magnetotail, such as the asymmetries of the cross-tail current sheet thickness and the occurrence of flux ropes, dipolarization events and energetic electron injections. In order to obtain a global pictures of Mercury's magnetotail dynamics and the relationship between these asymmetries, we perform global simulations with the magnetohydrodynamics with embedded particle-in-cell (MHD-EPIC) model, where Mercury's magnetotail region is covered by a PIC code. Our simulations show that the dawnside current sheet is thicker, the plasma density is larger, and the electron pressure is higher than the duskside. Under a strong IMF driver, the simulated reconnection sites prefer the dawnside. We also found the dipolarization events and the planetward electron jets are moving dawnward while they are moving towards the planet, so that almost all dipolarization events and high-speed plasma flows concentrate in the dawn sector. The simulation results are consistent with MESSENGER observations.

1 Introduction

MESSENGER has provided plenty of valuable information about Mercury's magnetosphere in the last decade, which have improved our understanding of the dynamics in the Mercury's magnetosphere. For examples, observations from MESSENGER have shown that the magnetospheric substorms at Mercury exhibit similar global magnetopheric configurations as the substorms at Earth, but in a time scale of 2 to 3 minutes, which is much shorter than the 2 to 3 hours of Earth's substorm (Slavin et al., 2010; Sun et al., 2015). MESSENGER has also observed magnetic structures that are closely related to magnetic reconnection, such as the flux transfer events near the magnetopause (Slavin et al., 2009; Slavin, Imber, et al., 2012), flux ropes or dipolarization fronts in the plasma sheet (DiBraccio et al., 2015; Slavin, Anderson, et al., 2012; Sun et al., 2016, 2015). These structures are similar to those in Earth's magnetosphere. However, at the same time, MESSENGER also found that several features are different from those of Earth. One of the most prominent puzzles raised by MESSENGER observations is the dawn-dusk asymmetry of Mercury's magnetotail.

Analyses of the MESSENGER data show that the energetic electrons or X-ray induced by energetic electrons on the nightside were more frequently observed in the post-midnight region, i.e., the dawnside, than in the premidnight region, i.e., the duskside (Baker

et al., 2016; Dewey, Slavin, Raines, Baker, & Lawrence, 2017; Ho et al., 2016; Lindsay et al., 2016). The dawnward drifting of the electrons may explain the energetic electrons dawn-dusk asymmetry (Lindsay et al., 2016). However, the study of magnetic reconnection related magnetic structures, which are flux ropes and dipolarization fronts, in the near-Mercury-neutral-line region showed both structures are also more frequently observed on the dawnside than on the duskside, which suggests the magnetic reconnection may prefer to happen on the dawnside and therefore created more energetic electrons in the postmidnight region than in the premidnight region [(Sun et al., 2016) see also, (Smith, Slavin, Jackman, Poh, & Fear, 2017; Sun et al., 2017)]. The dawnside magnetic reconnection preferentially occurrence in Mercury's plasma sheet is different from the observations in Earth's magnetosphere, where the magnetic reconnection related dynamic processes, such as the flux ropes (Imber, Slavin, Auster, & Angelopoulos, 2011) and dipolarization fronts (J. Liu, Angelopoulos, Runov, & Zhou, 2013), prefer the duskside plasma sheet. In addition, Poh et al. (2017a) found Mercury's magnetotail current sheet is thicker on the dawnside than the duskside, and it is believed that it is easier to trigger magnetic reconnection in a thinner current sheet. The relationship between the current sheet thickness and the reconnection products observations still needs to be explored. It has also been observed that there are more heavy ions (Na^+ and O^+) on the duskside plasma sheet than in the dawnside plasma sheet (Gershman et al., 2014; Raines et al., 2013). The role of the heavy ions in the magnetic reconnection is still largely unknown.

Since the satellite observations usually localize to a small region of the whole magnetosphere at a given time, it is difficult to recover the timing sequence and the global picture of the magnetospheric dynamics from the localized data alone. Numerical models, especially global models, can provide unique insight into these problems. Dorelli, Glocer, Collinson, and Toth (2015) studied the asymmetries introduced by the Hall effect in the global structure of Ganymede's magnetosphere, and suggested the Hall effect may also play an important in Mercury's magnetosphere. Lin, Wang, Lu, Perez, and Lu (2014), Lu et al. (2016) and Lu, Pritchett, Angelopoulos, and Artemyev (2018) have used a global hybrid model and a local PIC model to study the dawn-dusk asymmetry of Earth's magnetosphere. They found that the Hall effect transports the current sheet plasma and the magnetic flux from the dusk sector to the dawn sector. The transportation reduces duskside current sheet thickness, thus reconnection is easier to be triggered on the duskside. This explanation may work for Earth, but there are some difficulties to adopt it for Mer-

cury. Mercury's current sheet is thinner (Poh et al., 2017a) on the duskside, which is similar to the Earth and might be explained by the Hall effect. However, Mercury's reconnection products prefer the dawn sector. Recently, Y.-H. Liu et al. (2019) used box PIC simulations to study the magnetic reconnection preference for a thin current sheet that is embedded into a thick current sheet, and they found there is a suppression region on the ion drifting side, and therefore the reconnection prefers the electron drifting side, which might be applicable at Mercury.

A global numerical model of Mercury's magnetosphere is needed to solve these puzzles. Several numerical models have been used to study Mercury's magnetosphere in the past decades. BATS-R-US was the first MHD model applied for 3D global simulations of Mercury's magnetosphere (Kabin, Gombosi, De Zeeuw, & Powell, 2000; Kabin et al., 2008). Jia et al. (2015, 2019) developed the resistive body capability for BATS-R-US and studied how the induction effect that is arising from the conducting core affects the magnetospheric global response to the varying solar wind conditions. Multi-fluid MHD models that treat heavy ions as a separate fluid have been used for Mercury's magnetosphere simulations (Kidder, Winglee, & Harnett, 2008). Benna et al. (2010) studied Mercury's magnetosphere at the time of the first MESSENGER flyby with a Hall MHD model. Since the kinetic scales of Mercury's magnetospheric plasma can be comparable to Mercury's radius, kinetic effects may play an important role in Mercury's magnetosphere. To incorporate kinetic physics, hybrid models (Kallio & Janhunen, 2003; Müller et al., 2012; Travnicek et al., 2010; Wang, Mueller, Motschmann, & Ip, 2010), which treat the electrons as a massless charged fluid and model the ions as particles, test particle models, which trace the particle trajectories with a global electromagnetic field obtained from either a global numerical model (Schriver et al., 2011; Seki et al., 2013) or an analytic model (D. Delcourt, 2013; D. C. Delcourt et al., 2003), and particle-in-cell models (Schriver et al., 2017) have been applied to study Mercury's magnetosphere. Previous studies have presented some dawn-dusk asymmetric structures, for example, Müller et al. (2012) explained the formation of the 'double magnetopause' structure, which is asymmetric in the dawn-dusk direction, and Benna et al. (2010) showed the asymmetric ion drift belt in the inner magnetosphere. Due to the limitations of the physics capabilities or the grid resolutions of these models, the dawn-dusk asymmetries of the current sheet, magnetic reconnection and reconnection products of Mercury's magnetotail have not been studied in detail.

The MHD with embedded PIC (MHD-EPIC) model (Daldorff et al., 2014) makes it feasible to study Mercury's magnetotail dynamics with a realistic configuration. We use a PIC code to cover Mercury's inner tail, and the rest of the domain is handled by the MHD model BATS-R-US. The details of the numerical model are discussed in section 2. Section 3 provides the MESSENGER data that is used to compare with simulations in the later sections. The simulation results are presented and discussed in section 4 and section 5.

2 Numerical model

The MHD-EPIC model has been successfully applied to investigate the interaction between the Jovian wind and Ganymede's magnetosphere (Tóth et al., 2016; H. Zhou, Toth, Jia, Chen, & Markidis, 2019), Martian magnetotail reconnection (Ma et al., 2018) and Earth's dayside reconnection (Chen et al., 2017; Tóth et al., 2017). The MHD-EPIC model two-way couples the Hall MHD model BATS-R-US (Powell, Roe, Linde, Gombosi, & De Zeeuw, 1999; Tóth, Ma, & Gombosi, 2008) and the semi-implicit particle-in-cell code iPIC3D (Markidis, Lapenta, & Rizwan-Uddin, 2010) through the Space Weather Modeling Framework (SWMF) (Tóth et al., 2005, 2012). Recently, Chen and Tóth (2019) has developed the Gauss's Law satisfying Energy Conserving Semi-Implicit Method (GL-ECSIM), an improved version of the ECSIM (Lapenta, 2017), and implemented it into the iPIC3D code. This new PIC algorithm is used for all the MHD-EPIC simulations presented here.

For the MHD-EPIC simulations of Mercury's magnetosphere, we run the fluid code BATS-R-US first to reach a steady state, then we change to the time-accurate mode (Tóth et al., 2012) and couple the fluid model with the PIC code. Hall-MHD equations are solved by the fluid model for both MHD-EPIC simulations and pure Hall-MHD simulations. The simulation setup for both BATS-R-US and PIC are described in the following subsections.

2.1 Global MHD model: BATS-R-US

Following the work of Jia et al. (2015), a resistive body with finite conductivity layer is used to represent the interior structure of Mercury: the region within $r < 0.8\,R_M$ is the highly conducting core, and the layer between $0.8\,R_M$ and $1\,R_M$ with finite conduc-

tivity represents the mantle. The conductivity inside the mantle is set to be $\sim 10^{-7}\,S/m$. We refer to Jia et al. (2015) for more details about the conductivity profile.

The Hall effect and the electron pressure gradient term are also included in our generalized Ohm's law:

$$\mathbf{E} = -\mathbf{u}\times\mathbf{B} + \frac{\mathbf{J}\times\mathbf{B}}{q_e n_e} - \frac{\nabla p_e}{q_e n_e} + \eta\mathbf{J} \tag{1}$$

where q_e, n_e and p_e are the unsigned electron charge, electron number density (obtained from charge neutrality) and electron pressure, respectively. η represents the resistivity, which is the inverse of the conductivity and $\mathbf{J} = \nabla\times\mathbf{B}/\mu_0$ is the current density. The electron pressure is calculated from a separate equation:

$$\frac{\partial p_e}{\partial t} + \nabla\cdot(p_e\mathbf{u}_e) = (\gamma-1)(-p_e\nabla\cdot\mathbf{u}_e) \tag{2}$$

where $\gamma = 5/3$ is the adiabatic index, and $\mathbf{u_e} = \mathbf{u} - \mathbf{J}/(q_e n_e)$ is the electron velocity. In summary, the resistive Hall MHD equations with a separate electron pressure equation are solved in our MHD model.

Inside the mantle region ($0.8\,R_M < r < 1\,R_M$), there is no plasma flow, but the magnetic field still changes due to the finite conductivity. Only the reduced Faraday's law is solved inside the mantle:

$$\frac{\partial\mathbf{B}}{\partial t} = -\nabla\times(\eta\mathbf{J}). \tag{3}$$

Outside the planet surface, the whole set of MHD equations are solved. Since both the Hall term and the resistivity term are stiff, a semi-implicit scheme (Tóth et al., 2012) is used to speed up the simulations: the equations excluding the stiff terms are solved explicitly first, then the stiff terms are solved by an implicit solver.

The simulations are performed in the Mercury solar orbital (MSO) coordinates, where the X-axis is pointing to the Sun from Mercury, the Z-axis is parallel to Mercury's rotation axis, and the Y-axis completes a right-handed coordinate system. The whole simulation domain is a brick of $-64\,R_M < x < 8\,R_M$ and $-32\,R_M < y, z < 32\,R_M$ cut out from a spherical grid. The center of Mercury coincides with the origin of the coordinates. A dipole field with strength of 200 nT (Anderson et al., 2011) at the magnetic equator is used. The dipole axis is aligned with the Z-axis but the dipole center is shifted northward by $0.2\,R_M$. A stretched locally refined spherical grid is used. The tail region is refined so that the cell size is about $0.025\,R_M$ near $x = -2.5\,R_M$. The grid of the tail region is plotted in Figure 1(d). From our simulations, the plasma density in the lobes

is about 0.3 amu/cm^3, and the corresponding proton inertial length is about 420 km or $0.17\,R_M$. The Hall effect can be well resolved because one inertial length is covered by ~ 6 cells. The inner boundary condition for the magnetic field is applied at the interface of the mantle and the conducting core, where $r = 0.8\,R_M$ and the magnetic field is fixed due to the high conductivity. Since there is no plasma flow in the mantle, the inner boundary conditions for plasma density, velocity and pressure are applied on the planet surface $r = 1\,R_M$. A zero gradient boundary condition is applied to plasma density and pressure. The boundary condition for velocity is designed so that the plasma can be absorbed by the surface, and the surface is not an important source of plasma. For the inflow, a zero gradient boundary condition is applied to all velocity components. For the outflow, the radial velocity component is set to be zero at the boundary and a zero gradient boundary condition is applied to the tangential components. The plasma may flow around or flow into the surface, but it would not have a significant outflow component.

2.2 PIC model

The Gauss's Law satisfying Energy Conserving Semi-Implicit Method (GL-ECSIM) (Chen & Tóth, 2019) is used in the PIC region. MESSENGER observations suggest that the average near-Mercury neutral line (NMNL) is at around $x = -3\,R_M$ (Poh et al., 2017b; Slavin et al., 2009). To study Mercury's magnetotail reconnection, the tail region $-5.1\,R_M < x < -1.1\,R_M$, $-1.75\,R_M < y < 1.75\,R_M$ and $-0.5\,R_M < z < 1.5\,R_M$ is covered by the uniform Cartesian mesh of the PIC code (see Figure 1(a)). The cell size is $1/32\,R_M$ in all directions. 64 macro-particles per species per cell are used. In order to reduce the computational cost, an artificially reduced proton-electron mass ratio of $m_p/m_e = 100$ is set. The cell size is $\sim 1/5$ of the proton inertial length or twice of the plasma skin depth. The time step is 2.5×10^{-3} s, the maximum electron thermal speed is about 8×10^3 km/s, and the cell size is $1/32\,R_M$, so that the corresponding CFL number (the ratio of the time step to the cell crossing time by electrons) is about 0.25, which satisfies the 'accuracy condition' of the semi-implicit PIC methods (Markidis et al., 2010).

The grid resolution is not fine enough to capture all electron physics accurately, but it is sufficient to get the larger scale dynamics correctly. Chen and Tóth (2019) have performed a grid convergence study for a 2D reconnection problem, and it shows the simulation with 5 cells per ion inertial length produces correct reconnection rate, plasma

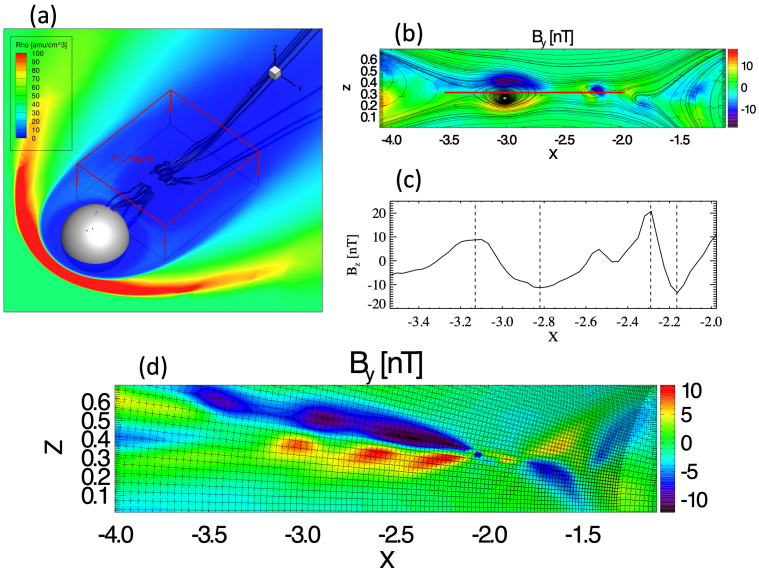

Figure 1. (a) The global structure of Mercury's magnetosphere at $t = 300\,s$ from the simulation MHD-EPIC-A. The mass density in the equatorial plane and the magnetic field lines of two flux ropes are shown. The red box is the region covered by the PIC code. It covers the whole tail region where magnetic reconnection may happen. In the Y-direction, the PIC region is close to but has not reached the magnetopause. (b) The Hall magnetic field B_y and magnetic field lines at $y = 0$ from MHD-EPIC-A. (c) The B_z component along the red line in (b). (d) The B_y field and the MHD grid of the Hall-A simulation at $y = 0$. The black crosses represent the cell centers of the stretched spherical grid. All the simulations presented in this paper use the same MHD grid.

flow and Hall magnetic field. It even produces the correct structures of the off-diagonal terms of the electron pressure tensor, even though the structures are diffusive (Figures 11 and 12 of Chen and Tóth (2019)).

3 MESSENGER observations in the nightside plasma sheet

This section provides observations of the proton properties and dipolarization fronts in Mercury's nightside plasma sheet from MESSENGER (Solomon, McNutt, Gold, & Domingue, 2007). The proton measurements are provided by the Fast Imaging Plasma Spectrometer (FIPS) (Andrews et al., 2007) and the magnetic field measurements are provided by the magnetometer (Anderson et al., 2007). FIPS could measure ions in an effective field of view of $\sim 1.15\pi$ sr with an energy range from ~ 46 eV/e to ~ 13.7

keV/e with a time resolution of $\sim$ 10 s. The magnetic field data are provided with a time resolution of 20 vectors per second and are under Mercury solar magnetospheric coordinates (MSM). In the MSM, the X_{MSM} is sunward, the Z_{MSM} is northward and parallel to the dipole axis, and the Y_{MSM} completes the right-handed system. The MSM coordinates and MSO coordinates are parallel with each other, but the MSO origin is the center of Mercury and the MSM origin centers on the Mercury dipole. The spacecraft position data are provided to be in the same time resolution as the magnetic field measurements, but they are aberrated according to the solar wind velocity and Mercury's orbital motion to make the X'_{MSM} antiparallel to the solar wind. The aberration changes the positions in the $X_{MSM} - Y_{MSM}$ plane, but does not change Z_{MSM}.

3.1 Proton properties

Proton density and pressure shown in Figure 2 were derived from one minute average distributions of protons under the assumption that they are isotropic and stationary Maxwellian distributions (Gershman et al., 2013; Raines et al., 2013, 2011). The proton moments derived from this method were applied in several studies on the plasma sheet dynamics (Gershman et al., 2014; Poh et al., 2018; Raines et al., 2011; Sun et al., 2017, 2018). The proton density distribution (left figure in Figure 2) shows clear dawn-dusk asymmetry with proton densities higher on the dawnside ($\sim$ 6 to 8 amu/cc) than on the duskside ($\sim$ 2 to 4 amu/cc). The dawn-dusk asymmetry of proton pressure (right figure in Figure 2) is not that prominent as proton density. The proton pressure shows weak dawn-dusk asymmetry in the downtail region ($X'_{MSM} < -1.3\ R_M$) with proton pressure on the dawnside plasma sheet slightly higher than on the duskside. This dawn-dusk asymmetry becomes more prominent in the near tail region with ($X'_{MSM} \sim -1\ R_M$), where proton pressure was from 1.3 to 1.7 nPa on the dawnside plasma sheet and was from 0.6 to 1.3 nPa on the duskside plasma sheet.

Korth et al. (2014) showed the distribution of mean proton flux in the nightside plasma sheet of Mercury. In that study, the mean proton flux showed clear dawn-dusk asymmetry with the flux much higher on the dawnside than on the duskside, which is similar to the distribution of proton density in Figure 2.

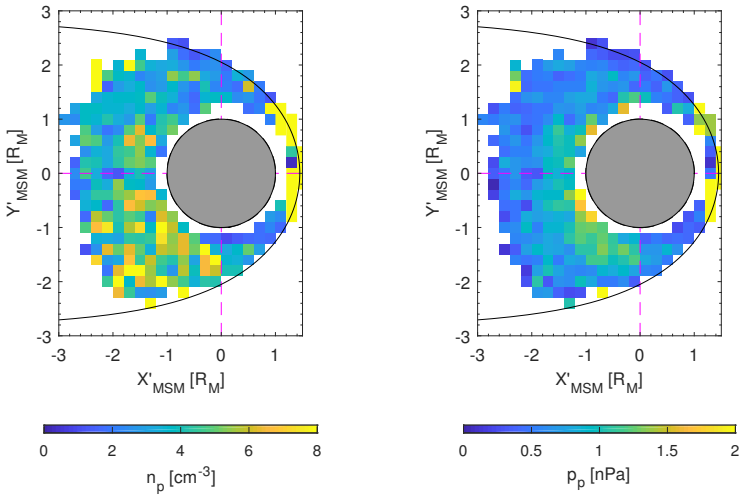

Figure 2. The MESSENGER observed proton density (left) and proton pressure (right) around the magnetic equator ($|Z_{MSM}| < 0.2R_M$). This figure shows the one minute proton moments derived from FIPS during the entire MESSENGER orbits around the Mercury (from 17 March 2011 to 30 April 2015). The black curve on both figures is the average location of the magnetopause (Winslow et al., 2013). The number of events in each bin is required to be larger than 3. The size of bin is 0.2 $R_M \times 0.2$ R_M. The colors indicate the intensity of density (left) and pressure (right), respectively.

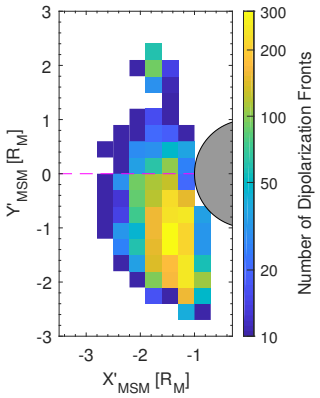

Figure 3. The spatial distribution of the dipolarization fronts observed by MESSENGER around the magnetic equator ($|Z_{MSM}| < 0.2R_M$). The size of bin is 0.3 R_M × 0.3 R_M. The color indicates the number of dipolarization fronts in each bin. The number of dipolarization fronts in each bin is required to be at least 3.

3.2 Dipolarization fronts

Dipolarization front, also called reconnection front, is defined as the leading edge of planetward travelling plasma flow burst, which is highly correlated with the magnetic reconnection [e.g., (Angelopoulos et al., 2013)]. In previous studies at Mercury, Sun et al. (2016) has shown clear dawn-dusk asymmetry of dipolarization fronts in the near-Mercury-neutral-line region with more dipolarization fronts on the dawnside plasma sheet than on the duskside plasma sheet. The following studies on the dipolarization fronts in the near-Mercury plasma sheet, proton energization and heating, energetic electrons and proton bulk flows have shown the similar dawn-dusk asymmetries (Dewey, Raines, Sun, Slavin, & Poh, 2018; Dewey et al., 2017; Sun et al., 2017).

Figure 3 shows the distribution of dipolarization fronts in Mercury's nightside plasma sheet. This figure contains the dipolarization fronts during the entire period MESSENGER orbited around Mercury. The dipolarization fronts were obtained according to the similar procedure as Sun et al. (2016). Since the dipolarization fronts were constrained in the regions with $Z_{MSM} < 0.2\ R_M$ and MESSENGER orbits were evenly distributed in the dawn-dusk direction (Sun et al., 2016), the occurrence rate of dipolarization fronts shows essentially the same structures as Figure 3. In the downtail region ($X'_{MSM} < -2\ R_M$), the dipolarization fronts show dawn-dusk asymmetry with more events on the dawnside plasma sheet than on the duskside, which is similar to (Sun et al., 2016). The dawn-dusk asymmetry becomes more prominent in the region closer to the planet (from $-2\ R_M$ to $-1\ R_M$).

4 Simulation results

We perform pure Hall-MHD and MHD-EPIC simulations with different upstream solar wind conditions. In order to avoid introducing dawn-dusk asymmetries from the solar wind, the Y-components of the IMF and the solar wind velocity are eliminated in all simulations. Since the Y-component of the velocity is zero, there is not need to apply aberration to the simulation results. The detailed solar wind parameters are shown in Table 1. Compared to the parameters used by Jia et al. (2015), we use a proton and electron temperature of 7.5 eV, which is half of the proton temperature of Jia et al. (2015). Since the total pressure of the solar wind is split between electrons and protons in this paper, the total plasma thermal pressure is still the same as Jia et al. (2015). The strength

of the IMF in both MHD-EPIC-A/Hall-A and MHD-EPIC-B/Hall-B is $|\mathbf{B}| = 19.4$ nT, which are also the same as Jia et al. (2015). The plasma parameters for MHD-EPIC-A/Hall-A is typical at Mercury's ambient space environment. The IMF configuration of MHD-EPIC-A/Hall-A is similar to a typical Parker spiral magnetic field, except that the B_y component is set to be zero and a negative B_z component is introduced to drive Mercury's magnetosphere. The IMF of MHD-EPIC-B/Hall-B purely consists of a negative B_z component with larger magnitude, which is a stronger driver than that of MHD-EPIC-A/Hall-A. We run the MHD code first to reach a steady state, then we run the time-accurate MHD-EPIC or Hall-MHD for 300 s, which is about 2 to 3 Dungey cycles of Mercury's magnetosphere (Slavin et al., 2009). It usually takes a numerical model a few Dungey cycles to settle down to a steady or quasi-steady state.

In the following subsections, we introduce the global picture of the simulation results first. Then the dawn-dusk asymmetry is discussed based on the simulations. We will briefly compare the MHD-EPIC simulations with the pure Hall-MHD simulations as well.

Table 1. The solar wind parameters in MSO coordinates.

Simulation ID	ρ [amu/cc]	Temperature [eV]	Velocity km/s	IMF [nT]
MHD-EPIC-A/Hall-A	40	7.5	(-400, 0, 0)	(-17.4, 0, -8.5)
MHD-EPIC-B/Hall-B	40	7.5	(-400, 0, 0)	(0, 0, -19.4)

4.1 Global picture

The global structure of Mercury's magnetosphere at $t = 300\,s$ from the simulation MHD-EPIC-A is shown in Figure 1. The equatorial plane is colored by the plasma mass density. It happens to have two flux ropes at this moment. By checking the time series of the simulation results, it is easy to figure out that the flux rope far from the planet is moving tailward, and the one near Mercury is moving planetward. These flux ropes are produced by the PIC code, which covers most parts of the inner magnetotail. In the Y-direction, the PIC region is close to but has not reached the magnetopause. Figure 1

shows a typical state of the MHD-EPIC-A simulation. Magnetic reconnection happens around $x = -2.5\,R_M$, and produces tailward and planetward moving flux ropes.

A 2D cut at y = 0 is presented in Figure 1(b) to show more details of these two flux ropes. The bipolar B_y field is the remnants of the reconnection Hall magnetic field. There is no significant core field for either flux ropes at this moment due to the lack of IMF B_y, which may act as core field seed during the formation of a flux rope. Compared to a typical flux rope with a strong core field, these two flux ropes presented here are more like collections of O-lines. The tailward flux rope is about $1\,R_M$ long in the Y-direction, and the planetward one is about $0.5\,R_M$ long. The flux rope diameter measured by the B_z field peak-to-peak distance in the X-direction is about $0.3\,R_M$ (730 km) for the tailward one and $0.15\,R_M$ (360 km) for the planetward one (Figure 1(c)). DiBraccio et al. (2015) estimates the mean flux rope diameter to be $0.14\,R_M$ (345 km) by using the Alfven speed of 465 km/s times the time delay between MESSENGER detecting the two B_z peaks. Our simulations suggest the typical ion jet velocity is about 1000 km/s (Figure 10). The mean diameter of the MESSENGER observed flux ropes will be about $0.3\,R_M$ if 1000 km/s instead of 465 km/s is used in the estimation. In any case, the diameters of the two flux ropes in Figure 1 are similar to the MESSENGER observations. Across the flux ropes, B_z changes from 10 nT to -10 nT for the tailward one and from 20 nT to -15 nT for the planetward one. These B_z peak-to-peak amplitudes are close to the average of MESSENGER observation value of 20 nT (DiBraccio et al., 2015). Inside the flux rope, the proton density is about 1.5 amu/cc in the simulation, while the median observed density is 2.03 amu/cc (DiBraccio et al., 2015).

The agreement of the flux rope properties between the MHD-EPIC-A simulation and MESSENGER observations demonstrates that our mode behaves reasonably well in capturing Mercury's magnetotail reconnection. In the following subsections, we will examine the dawn-dusk asymmetries of Mercury's tail.

4.2 Tail current sheet thickness and plasma profile

Poh et al. (2017a) calculated the current sheet thickness from hundreds of MESSENGER crossings, and they found the current sheet is thinner on the duskside (+Y) than the dawnside (-Y) on average. Using the same fitting method described by Poh et al. (2017a), we calculate the current sheet thickness from our simulations. The B_x field

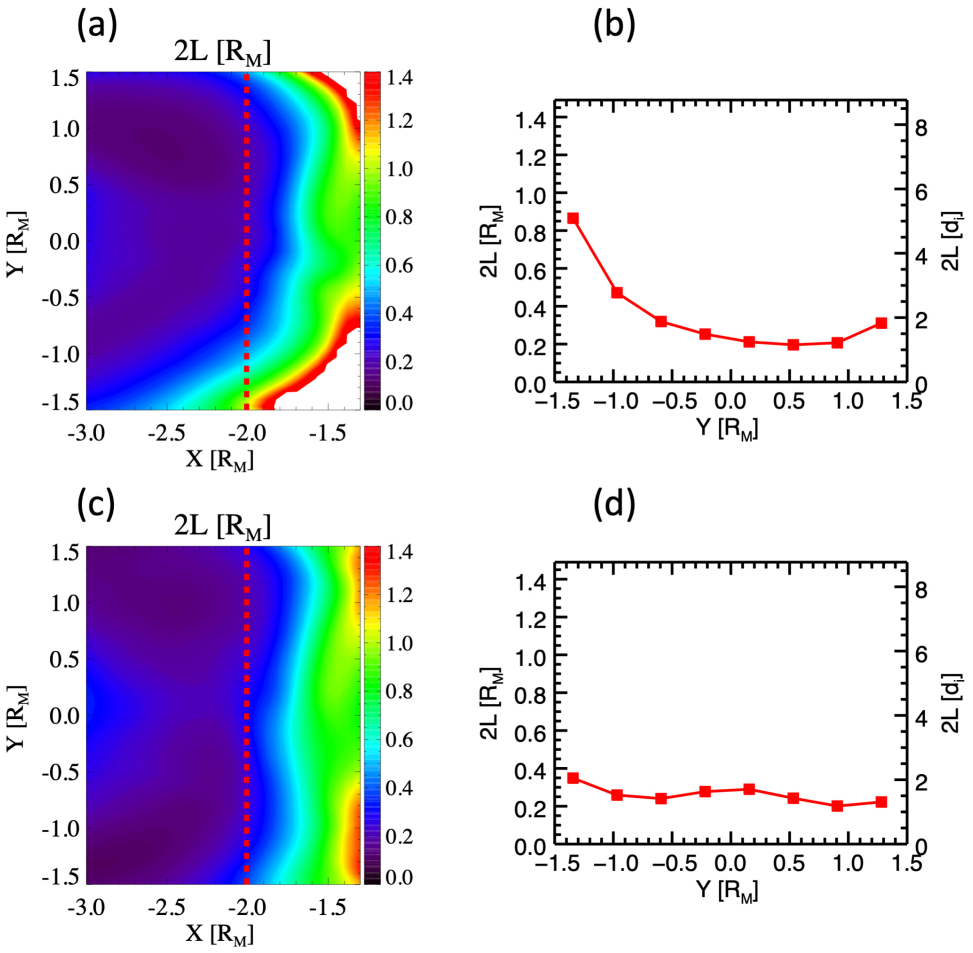

Figure 4. The time-averaged current sheet thickness of MHD-EPIC simulations. (a) and (c) correspond to the MHD-EPIC-A and MHD-EPIC-B runs, respectively. (b) and (d) are the thickness at $x = -2\,R_M$, which is marked by the red dashed lines in (a) and (c). The right Y-axes of (b) and (d) are the thickness normalized with $d_i = 0.17\,R_M$, which corresponds to a typical density of 0.3 amu/cc.

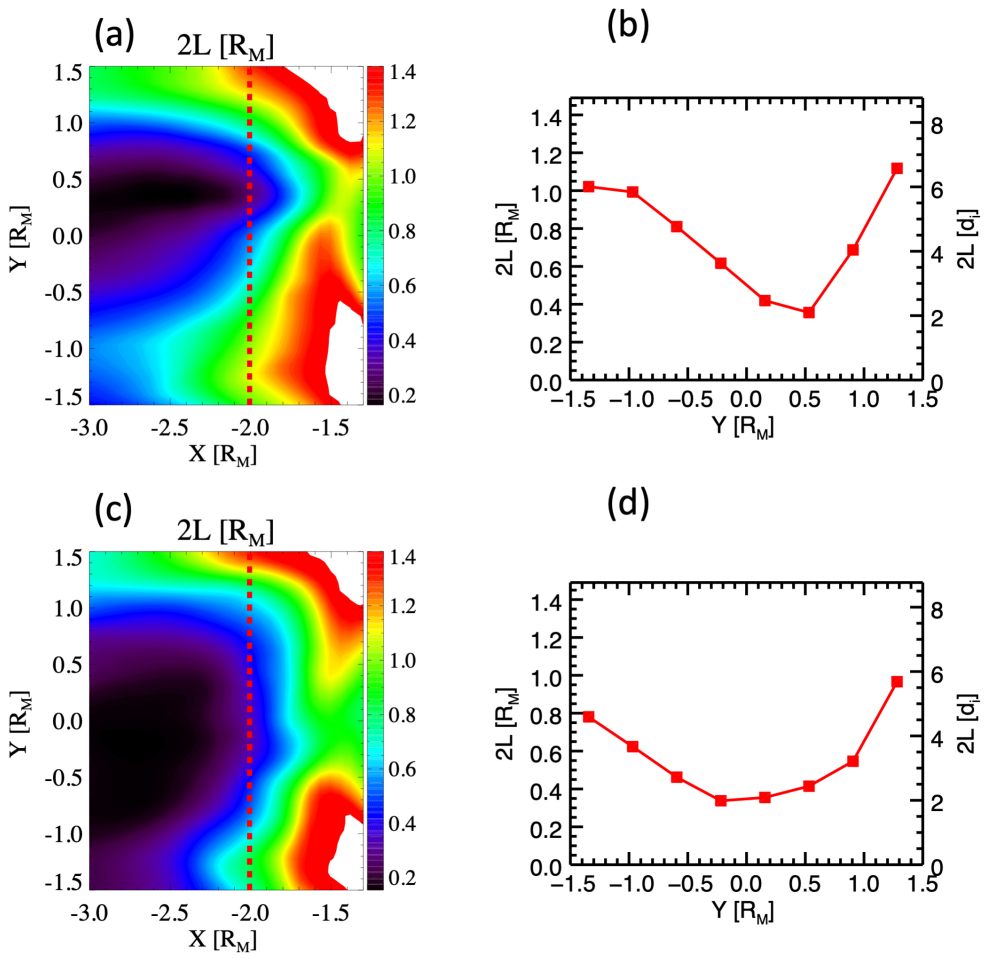

Figure 5. The current sheet thickness of Hall-A ((a) and (b)) and Hall-B ((c) and (d)) simulations. (b) and (d) are plots of current sheet thickness at $x = -2\,R_M$. The right Y-axes of (b) and (d) are the thickness normalized with $d_i = 0.17\ R_M$, which corresponds to a typical density of 0.3 amu/cc.

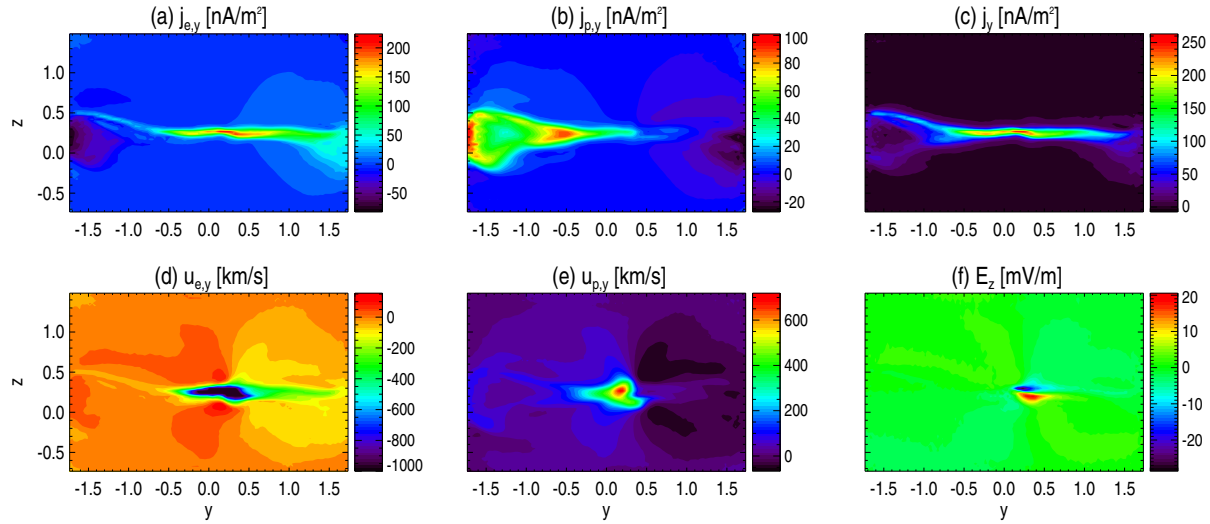

Figure 6. The 300-second average current sheet structure of MHD-EPIC-A at $x = -2\,R_M$. (a), (b) and (c) are the electron current, proton current and total current in the Y-direction, respectively. (d) is the electron velocity in the Y-direction. It can be as fast as -4,000 km/s, and we make the color saturated at -1,000 km/s to show more structures. (e) is the proton velocity in the Y-direction. (f) is the electric field in the z-direction.

along the Z-axis is fitted to a one-dimensional Harris current sheet model:

$$B_x(z) = B_0 \tanh\left(\frac{z - z_0}{L}\right). \tag{4}$$

The fitted current sheet thickness is 2L. The fitting is done every 2 s, and its average over 300 s is shown in Figure 4.

Figure 4(a) shows that the center of the thin current sheet of MHD-EPIC-A is shifted to the dusk (+Y) direction. The proton density of the thin current sheet around $x = -2\,R_M$ is about 0.4 amu/cc, and it can be as low as 0.02 amu/cc in the ambient lobe. The proton inertial length d_i of a density of 0.4 amu/cc is $0.15\,R_M$, which is the same order as the current sheet thickness in Figure 4. A cut of thickness at $x = -2\,R_M$ is presented in Figure 4(b). It is clear to see that the current sheet is thicker on the dawnside (-Y) than the duskside (+Y), which is consistent with the profile obtained from MESSENGER data. Figure 4(b) of Poh et al. (2017a) shows the current sheet thickness from hundreds of current sheet crossings. For this MESSENGER plot, the corresponding solar wind conditions are unknown and may vary a lot, and it contains current sheet crossings from $x = -3.0\,R_M$ to $x = -1.1\,R_M$, so the thickness may vary from $0.1\,R_M$ to $1\,R_M$ even for the same Y coordinate. But the mean current sheet thickness is probably able to represent the status under a typical solar wind condition. In the observation plot, the thinnest average current sheet is about $0.3\,R_M$, and it increases to about $0.7\,R_M$ on the dawnside and $0.5\,R_M$ on the duskside. Since $x = -2\,R_M$ is roughly the middle point of the MESSENGER crossings distribution in the X-direction, we plot the current sheet thickness at $x = -2\,R_M$ in Figure 4(b). The current sheet can be as thin as $0.2\,R_M$, which is about 1 d_i, and it increases to $0.8\,R_M$ at $y = -1.5\,R_M$ and $0.3\,R_M$ at $y = 1.5\,R_M$. The MHD-EPIC-A simulation current sheet is slightly thinner than the observations around midnight and in the dusk sector. Considering the large variance in the MESSENGER data (Figure 4(b) of Poh et al. (2017a)), the simulation agrees with observations very well.

The current sheet thickness for MHD-EPIC-B, which is driven by $B_z = -19.4$ nT IMF, is presented in Figure 4(c) and (d). The current sheet that is far away from the midnight becomes thinner than in the MHD-EPIC-A simulation, because the stronger dayside magnetic reconnection transports more magnetic flux to the tail to produce higher magnetic pressure. The thickness becomes less asymmetric than MHD-EPIC-A, even though

the dawnside current sheet is still slightly thicker than the duskside. The bump near the midnight is probably produced by the thick current sheet of the reconnection exhaust.

We repeat the same analysis of the current sheet thickness for the two Hall-MHD simulations using the same input parameters as those in the MHD-EPIC simulations. The results are shown in Figure 5 for comparison. The current sheet thickness at X = -2 R_M in the Hall MHD simulations is significantly larger compared to the MHD-EPIC simulation results and the MESSENGER observations. It can be seen that the current sheet thickness is not symmetric around midnight in the Hall-MHD simulations, either, and the thinnest part of the tail current sheet is displaced towards dusk (+Y), which is similar to that seen in the MHD-EPIC simulations. These results together suggest that the asymmetry is likely to be related to the Hall effect.

The cross-tail current density of MHD-EPIC-A at $x = -2\,R_M$ is presented in Figure 6. The duskside (+Y) electron current density is larger than the dawnside (-Y), but the proton current density is larger on the dawnside (-Y). The maximum current density of $j_y \approx 200\,\mathrm{nA/m^2}$ arises around midnight, and it reduces to less than $100\,\mathrm{nA/m^2}$ on the two flanks. The thin current sheet extends farther in the dusk sector (+Y) than the dawn sector. The spatial variation of the total current density j_y presented here is consistent with MESSENGER observations (Figure 4(c) of Poh et al. (2017a)).

Figures 7 to 9 show the time-averaged profiles of various plasma properties on the current sheet surface for MHD-EPIC-A, MHD-EPIC-B and Hall-A, respectively. The plots of Hall-B are not shown, because they are not significant difference than Hall-A in terms of the properties we discussed below. The current sheet surface is defined as the surface where B_x changes sign, and its projection into the X-Y plane is shown in the figures. All three simulations show significant dawn-dusk asymmetries of plasma density, electron pressure and total pressure. In the inner magnetotail, at a radial distance of $\sim 1.5\,R_M$ from the center of Mercury, the dawnside (-Y) plasma density (6 amu/cc for MHD-EPIC-B, and 10 amu/cc for MHD-EPIC-A/Hall-A) is about twice of the duskside (+Y) density (3 amu/cc for MHD-EPIC-B, 5 amu/cc for MHD-EPIC-A, and 7 amu/cc for Hall-A). Both the density values and the dawn-dusk ratio are close to the MESSENGER observation (Figure 2). By studying Earth's magnetotail, Lin et al. (2014) and Lu et al. (2016) found that before the onset of magnetic reconnection, there is more plasma in the dawn sector of Earth's magnetotail due to the $\mathbf{E}\times\mathbf{B}$ drift caused by the Hall elec-

tric field. Figures 7 to 9 presented here are averages of dynamic current sheets, where reconnection occurs frequently, instead of the status before the reconnection onset. However, the Hall effect is the only mechanism that could produce dawn-dusk asymmetry in the Hall-A simulation, so that the Hall effect must be the reason to create higher dawnside plasma density in Hall-A as well as the MHD-EPIC simulations. Figure 6(f) shows that the average E_z component of MHD-EPIC-A is stronger on the dusk side, which is a key for the $\mathbf{E}\times\mathbf{B}$ drift explanation and is consistent with Lin et al. (2014), Lu et al. (2016) and Lu et al. (2019). The MESSENGER data indicates slight proton pressure enhancement on the dawnside (Figure 2(b)), but our simulations do not show any significant preference of the proton pressure. The simulated electron pressure and hence the total pressure are higher on the dawnside (-Y). Eq. (2.1) is the electron pressure equation solved by the Hall-MHD model, and its right-hand side, the compression term, can produce the dawnside pressure enhancement. Because the $u_{e,z}$ component is small and the $u_{e,x}$ component changes slowly in the X-direction, the $\frac{\partial u_{e,y}}{\partial y}$ term must contributes most to the compression $\nabla\cdot\mathbf{u}_e$. From Figure 6(d), we can see the electron velocity reduces shapely from a few thousand to less than 500 km/s near $y = 0.5\,R_M$. The braking of $u_{e,y}$ is consistent with the dawnside electron pressure enhancement. The amplitude of the proton velocity $u_{p,y}$ is much smaller than $u_{e,y}$, and so is the proton compression $\nabla\cdot\mathbf{u}_i$. This may explain why there is no significant proton pressure asymmetry. Larger dawnside (-Y) electron pressure and total pressure are also consistent with thicker dawnside (-Y) current sheet thickness.

4.3 Magnetic reconnection

We discuss the asymmetries that are directly related to the magnetotail reconnection in this section. The average proton reconnection jets on the current sheet surface are shown in Figure 10 for all simulations. In the MHD-EPIC simulations, there is no significant dawn-dusk asymmetry of the tailward jets. But it is clear that the planetward proton jets prefer the dawnside (-Y). In the Hall-A simulation, the reconnection jets center around $y = 0.5\,R_M$, which is consistent with the thin current sheet location (Figure 5). The Hall-B simulation does not show any significant dawn-dusk asymmetry of either tailward or planetward jets.

The evolution of the proton jet $u_{p,x}$, electron jet $u_{e,x}$ and magnetic field B_z in the current sheet center at $x = -2.9\,R_M$, $x = -2.3\,R_M$ and $x = -1.6\,R_M$ (the vertical

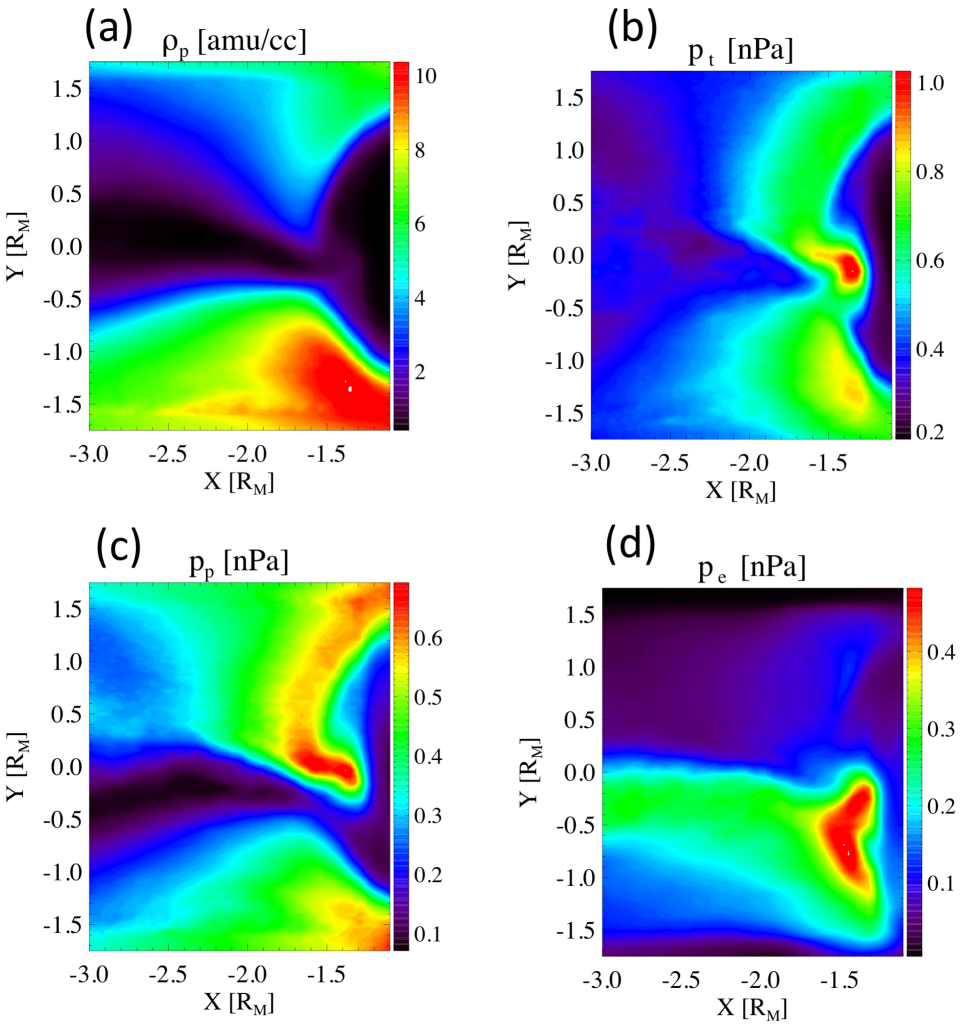

Figure 7. The time-averaged plasma profiles from the PIC output on the current sheet surface for MHD-EPIC-A: proton density (a), total pressure (b), proton pressure (c) and electron pressure (d).

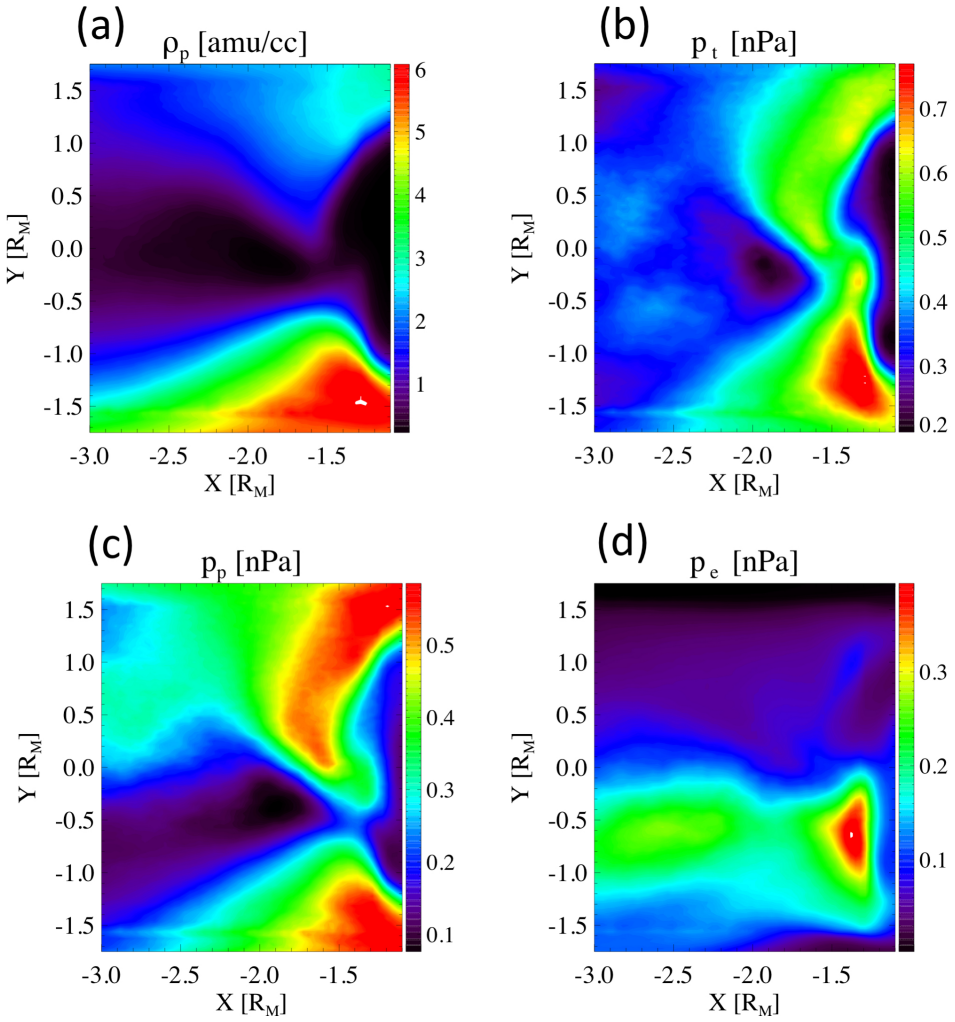

Figure 8. The time-averaged plasma profiles from the PIC outputs on the current sheet surface for MHD-EPIC-B.

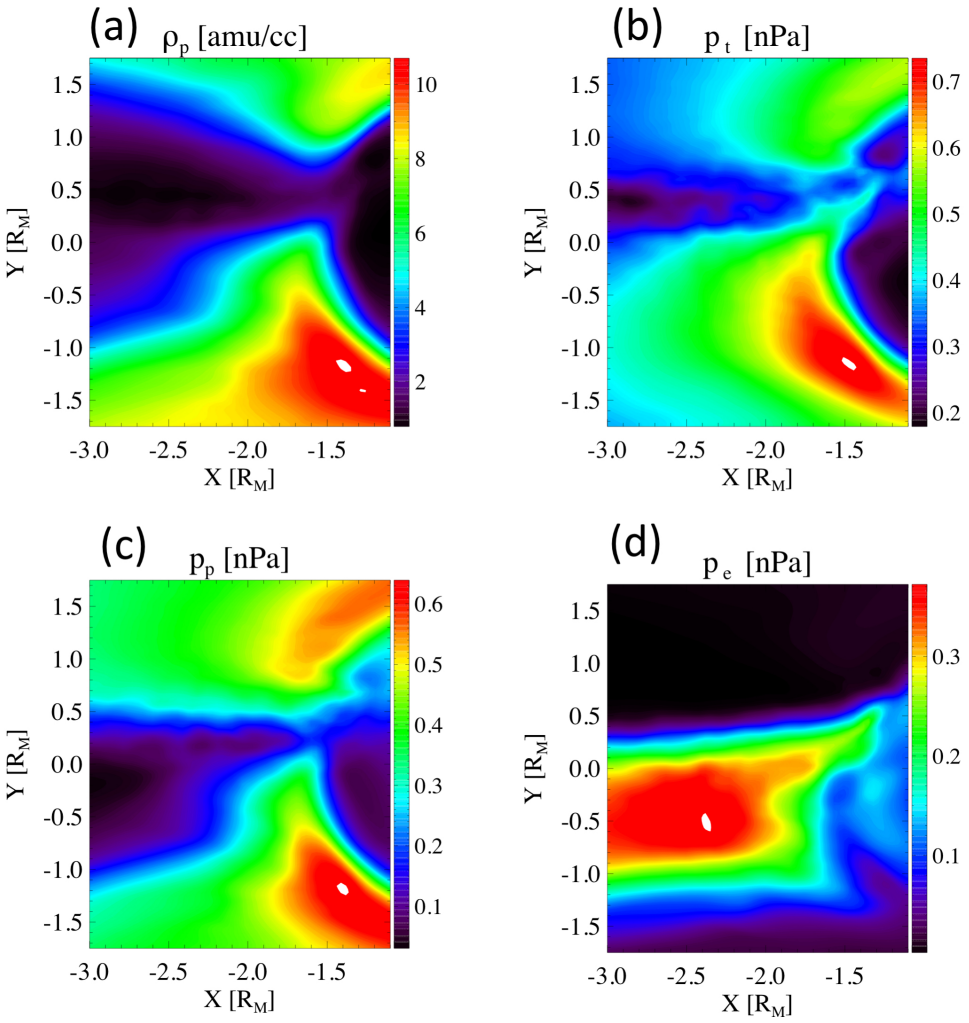

Figure 9. The time-averaged plasma profiles on the current sheet surface for Hall-A: proton density (a), total pressure (b), proton pressure (c) and electron pressure (d). The electron pressure presented here is calculated by a separate electron pressure equation in our MHD model.

lines in Figure 10(a)) are shown in Figure 11. $x = -2.9\,R_M$ and $x = -1.6\,R_M$ are in the tailward and planetward outflow regions, respectively. $x = -2.3\,R_M$ is close to the X-lines so that the jets can be either tailward or planetward. The plasma jets at $x = -2.3\,R_M$ indicate the location of X-lines. If we ignore the first 50 s of the simulation, which corresponds to the transition period of starting MHD-EPIC from a steady-sate Hall MHD configuration, the reconnection sites and the tailward jets prefer the dusk side slightly. For example, it is more frequent to observe electron jets for $y \in [0, 0.5]R_M$ than $y \in [-0.5, 0]R_M$ at $x = -2.3\,R_M$. However, on the planet side of the X-line, both the high-speed plasma jets $u_{p,x}$ and $u_{e,x}$, and the enhanced B_z shift to the dawnside. At $x = -1.6\,R_M$, there are neither proton nor electron jets found in the region $y > 0$.

The reconnection products with a strong IMF driver (MHD-EPIC-B) are presented in Figure 12. For this case, not only the planetward jets ($x = -1.6\,R_M$), but also the tailward jets ($x = -2.3\,R_M$) and the reconnection sites ($x = -2.0\,R_M$), which are inferred from the reconnection jets, prefer the dawn sector. For example, it is not unusual to see either proton jet $u_{p,x}$ or electron jet $u_{e,x}$ between $y = -0.5\,R_M$ and $y = -1.0\,R_M$ at $x = -2.3\,R_M$ and $x = -2.0\,R_M$, but it is rarer to have high-speed jets between $y = 0.5\,R_M$ and $y = 1.0\,R_M$ at the same X-coordinate.

The simulated spatial distributions of the plasma jets and enhanced B_z in the inner tail are consistent with MESSENGER observations. Figure 2 of Poh et al. (2017a) shows that the dawnside B_z field is stronger than the duskside, and the B_z field peaks at $y = -0.2\,R_M$. Our MHD-EPIC-A and MHD-EPIC-B simulations also show a peak value of $B_z \sim 30$ nT between $y = 0\,R_M$ and $y = -0.5\,R_M$ at $x = -1.6\,R_M$, and the dawnside B_z is larger than the dusk side as well. Dewey et al. (2017) found the energetic electron injections concentrate in the dawn sector, and the peak fraction of the dipolarization associated events occurs at LT $\sim$ 1-2, which corresponds to $y \sim 0.4$-0.9 for $x = -1.6\,R_M$. Our simulation results are consistent with the MESSENGER energetic particle observations. The simulation high-speed electron jets prefer to occur between $y = 0\,R_M$ and $y = -0.5\,R_M$ at $x = -1.6\,R_M$.

The MHD-EPIC simulations suggest that the closer to Mercury, the stronger the dawn-dusk asymmetries of the reconnection products are. Observational evidences for this pattern may already exist in the publications. Smith et al. (2017) used an automated method to identify flux ropes, and they observed a weak dawn-dusk asymmetry with 58%

of flux ropes observed in the dawn sector. Most of the flux ropes lie between 1.5 and 2.5 R_M down the tail. This statistical result suggests that the dawn-dusk asymmetry between $x = -1.5\,R_M$ and $x = -2.5\,R_M$ is not very strong. But the energetic electron spatial distribution by Dewey et al. (2017) shows that almost all injections are observed in the midnight-to-dawn sector. Even though these two papers discussed different phenomena, both phenomena are likely the products of magnetic reconnection. In order to further confirm this hypothesis, we plot the spatial distribution of the dipolarization fronts observed by MESSENGER in Figure 3, which shows strong dawn-dusk asymmetry, and there is a trend that the asymmetry is stronger in the region closer to Mercury. Figure 14 shows the evolution of a dipolarization event, which is characterized by B_z enhancement, from the MHD-EPIC-A simulation. The structure of enhanced B_z is circled by the red ovals on the plots. The dipolarization initially appears at $x \sim -2.3\,R_M$, and the majority of the structure is in the dusk sector. The enhanced B_z structure moves dawnward when it is moving towards Mercury. The electrons also move dawnward at $x < -1.5R_M$, and the electron flow streamlines are over-plotted above B_z. The dawnward velocity component of electrons is a natural consequence of the cross-tail current. If we assume that part of the dawnward moving electrons are frozen into the magnetic field lines, the motion of the dipolarization front can be explained as well. The protons around the dipolarization front are moving duskward in the current sheet (see the proton streamlines in Figure 14). However, the high-speed proton jets are more frequently observed in the dawn sector near Mercury, which is consistent with MESSENGER observations (Sun et al., 2017). Since both the dipolarization fronts and the high-speed protons prefer the dawnside, it is possible that the protons are accelerated by the dipolarization fronts (X.-Z. Zhou, Angelopoulos, Sergeev, & Runov, 2010). The details of the proton acceleration process and its dawn-dusk asymmetry needs to be clarified in the future.

In order to demonstrate the importance of including physics beyond Hall-MHD, we compare the MHD-EPIC simulations with pure Hall-MHD simulations. Figure 13 shows the evolution of plasma jets and B_z for Hall-B simulation. This simulation does not show any significant dawn-dusk asymmetry and the results are quite different from those of the MHD-EPIC-B run.

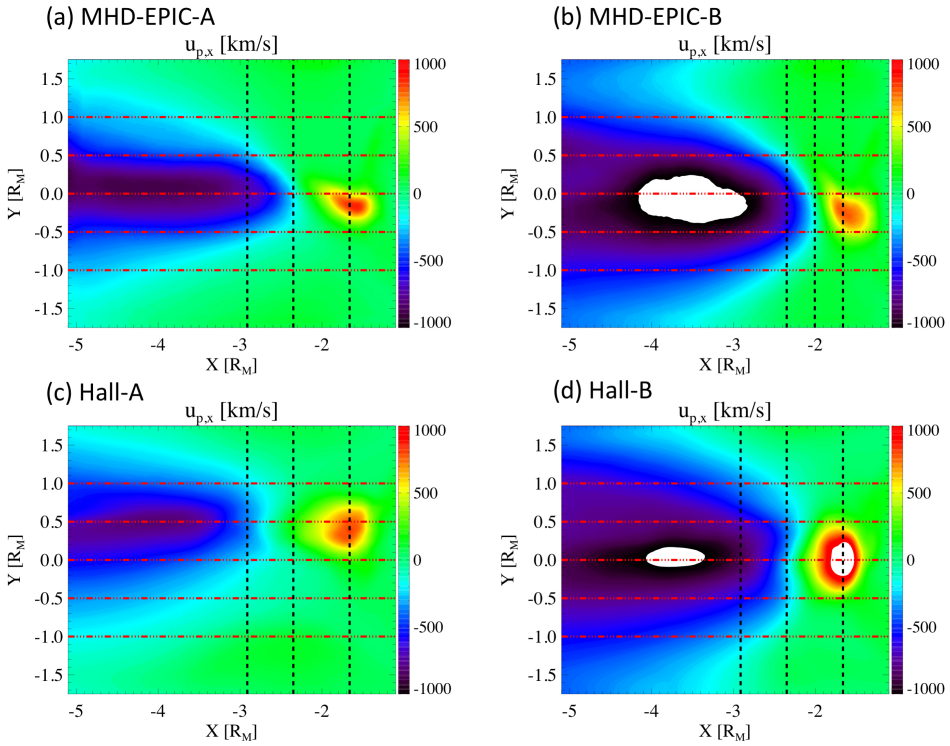

Figure 10. The time-averaged X-component of the proton velocity on the current sheet surface for the four simulations. The horizontal dashed lines are at $y = -1, -0.5, 0, +0.5$ and $+1\,R_M$, respectively. The location of the vertical black lines change from plot to plot. The time evolution along these vertical lines are shown in the following figures. The color range is saturated at 1000 km/s and -1000 km/s.

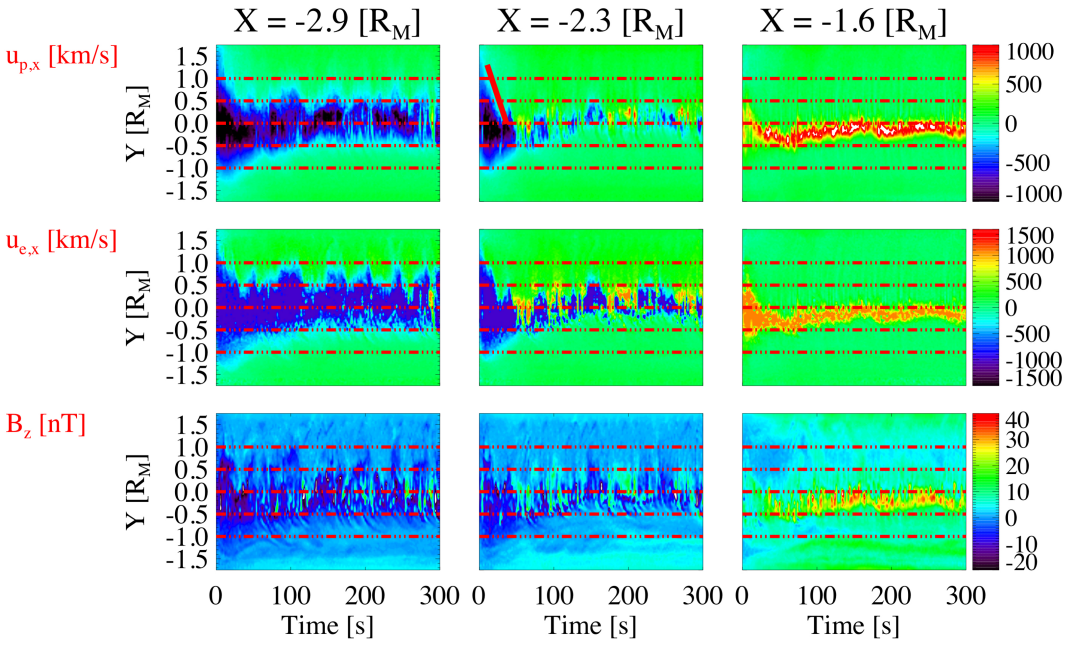

Figure 11. The evolution of different quantities on the current sheet surface at $x = -2.9\,R_M$, $x = -2.3\,R_M$ and $x = -1.6\,R_M$ (see the three vertical lines in Figure 10(a)) for the MHD-EPIC-A simulation. The time serials of the x-component of the proton velocity $u_{p,x}$, the x-component of the electron velocity $u_{e,x}$, and the B_z magnetic field from the beginning of the simulation to the end are displayed. The solid red line in the top middle plot is approximately parallel to the contour line of $u_{p,x}$ = -500 km/s. Its slope indicates the shrinkage of the X-lines.

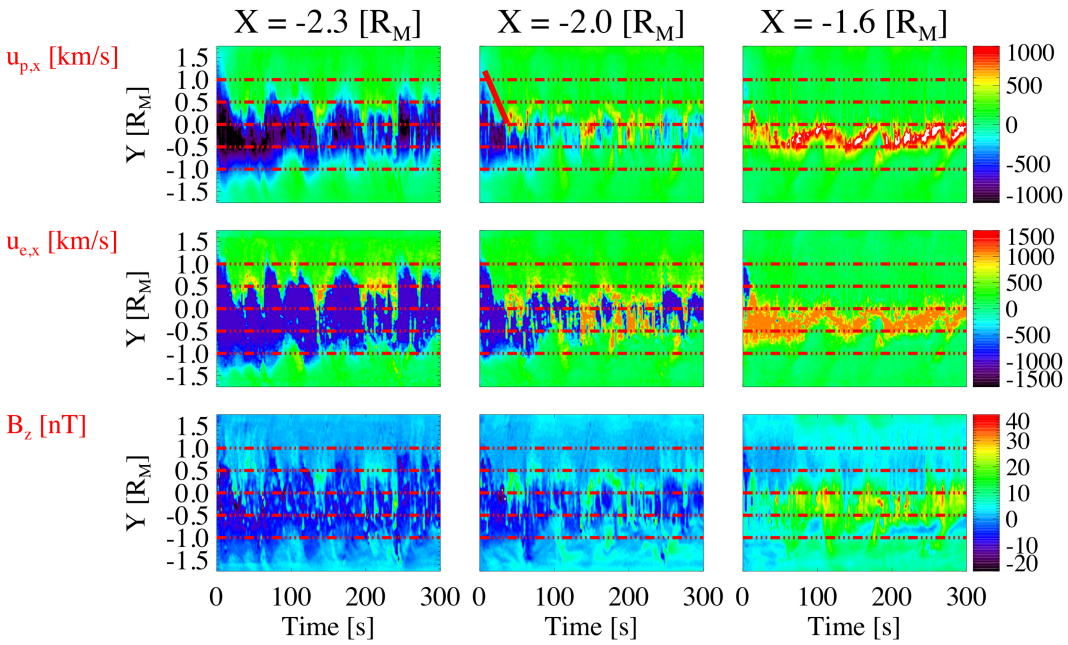

Figure 12. The same quantities as Figure 11 for the MHD-EPIC-B simulation at $x = -2.3\,R_M$, $x = -2.0\,R_M$ and $x = -1.6\,R_M$ (see the three vertical lines in Figure 10(b)).

5 Discussion

It is straightforward to track the evolution of the X-lines in the current sheets with simple geometries. However, it is difficult to directly track the onset and growth of an X-line automatically in MHD-EPIC simulations once the system is fully developed. We present where and when the reconnection related phenomena are observed in the simulations, such as Figure 11 and Figure 12, and infer the spatial distributions of the X-lines from the reconnection jets.

In the MHD-EPIC-A simulation, the IMF driver of $B_z = -8.5\,\mathrm{nT}$ is moderate, and the driver of MHD-EPIC-B is strong. These simulations suggest that Mercury's magnetotail reconnection sites slightly prefer the duskside (Figure 11) when the dawnside current sheet is significantly thicker than the duskside (Figure 4(a) and (b)) under a moderate IMF driver (MHD-EPIC-A), and the reconnection sites prefer the dawnside (Figure 12) when the dawnside current sheet is almost as thin as the duskside (Figure 4(c) and (d)) under a strong driver (MHD-EPIC-B). The results of MHD-EPIC-B simula-

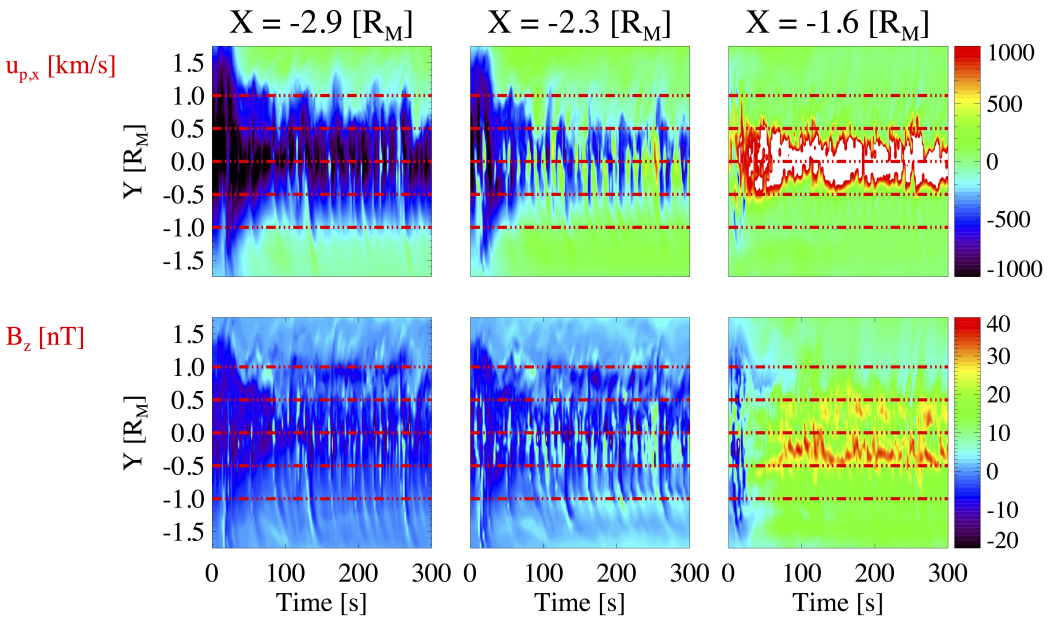

Figure 13. The evolution of the proton velocity $u_{p,x}$ and magnetic field B_z at $x = -2.9\,R_M$, $x = -2.3\,R_M$ and $x = -1.6\,R_M$ (see the three vertical lines in Figure 10(d)) of the current sheet of the Hall-B simulation.

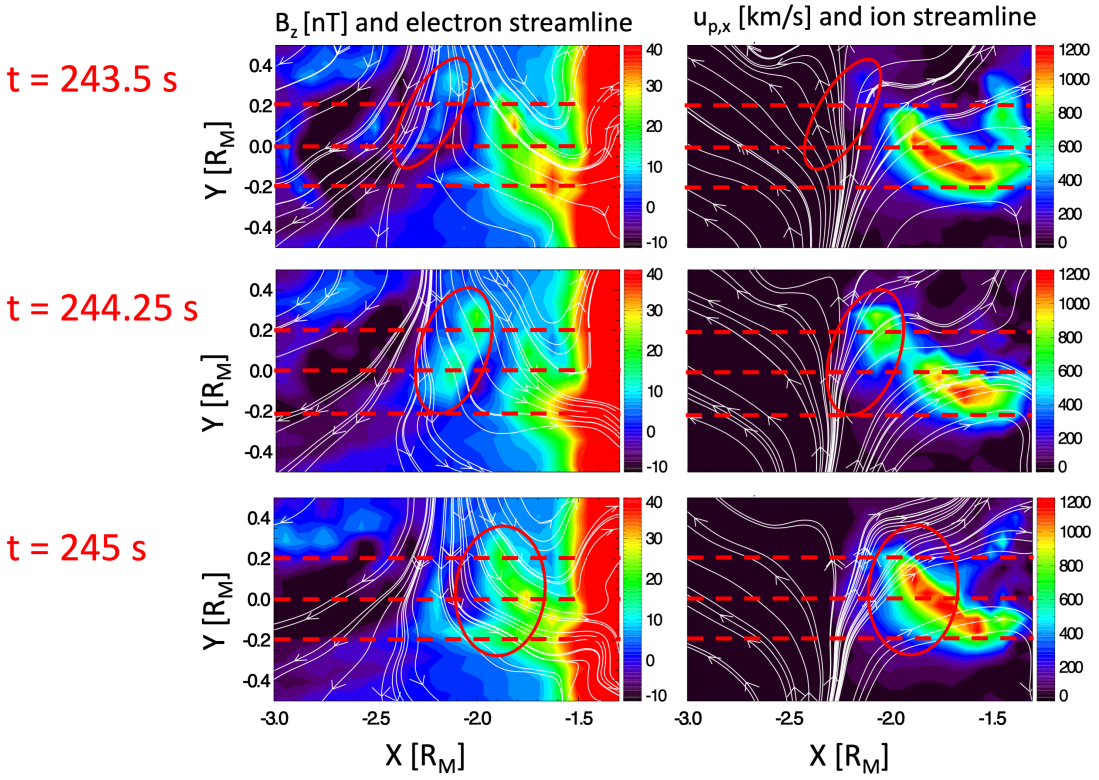

Figure 14. The B_z magnetic field and proton velocity $u_{p,x}$ on the current sheet surface at different times. The electron streamlines (the white lines) are overplotted on the B_z plots. The red ovals indicate the location of enhanced B_z.

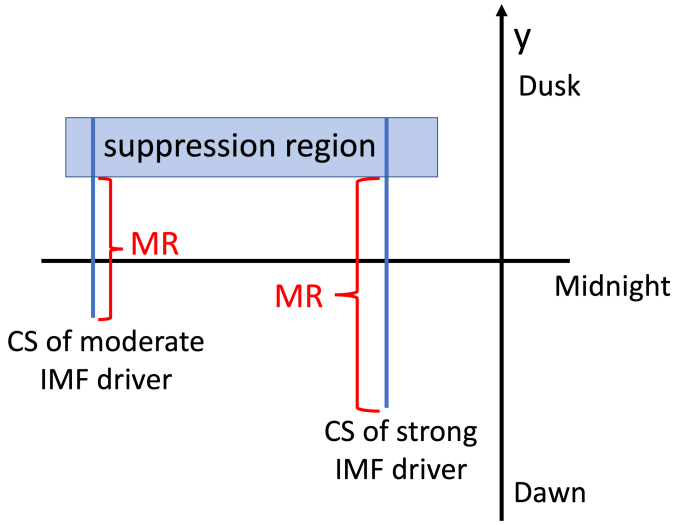

Figure 15. A cartoon illustrating the influence of the current sheet asymmetry and reconnection suppression region on the reconnection asymmetry for moderate and strong IMF driving conditions. The magnetic reconnection occurs in the region indicated with MR.

tion are consistent with what Y.-H. Liu et al. (2019) found in 3D box PIC simulations. They found that there is a reconnection 'suppression region' on the ion drifting side (the duskside in our simulations) of a thin current sheet, so that the magnetic reconnection prefers the electron-drifting side. Under a moderate driver, the majority of the thin current sheet lies on the duskside. For such current sheet configuration, even though part of the duskside current sheet is inactive, most of the reconnection sites may still be on the duskside, just as in the MHD-EPIC-A simulation. Since part of the duskside current sheet is inactive, the duskside preference of the reconnection should be weaker than the thin current sheet. We think this may be the reason why the MHD-EPIC-A simulation shows strong current sheet thickness asymmetry, but the reconnection preference is not significant. When the IMF driver is strong, such as in the case of MHD-EPIC-B, the current sheet is thin enough to allow magnetic reconnection to occur in almost the whole magnetotail current sheet, so that the dawn-dusk asymmetry of the current sheet thickness has little influence on the magnetic reconnection, and the suppression region (Y.-H. Liu et al., 2019) on the duskside determines the dawn-dusk asymmetry of the reconnection sites. Figure 15 displays the relative importance of the current sheet asymmetry and the reconnection suppression region. Besides the dawnside preference introduced by the 'suppression region', we find that the planetward moving electron jets and the dipolarization fronts are also shifted dawnward. The dawnward motion makes it rare to observe high-speed planetward plasma jets and dipolarization events in the dusk sector.

The IMF strength is the same for all simulations, but MHD-EPIC-A and Hall-A contain a significant B_x component. It is impossible to tell whether the difference between MHD-EPIC-A/Hall-A and MHD-EPIC-B/Hall-B comes from the IMF B_x or B_z. But it is clear that the dayside magnetopause reconnection rate of MHD-EPIC-B/Hall-B is faster than MHD-EPIC-A/Hall-A due to the larger B_z component in MHD-EPIC-B/Hall-B.

We now turn to the first 50 s of the MHD-EPIC simulations. Since it corresponds to the transition from the steady-state Hall-MHD to MHD-EPIC, the results of the first 50 s may not represent a typical state of Mercury's magnetotail. But it still provides interesting insights into Mercury's magnetotail reconnection. At the very beginning, MHD-EPIC inherits the current sheet structure from the steady-state Hall-MHD results. The Hall effect of the steady-state Hall-MHD exists, but it is weak due to the large numer-

ical diffusion. The current sheet thickness between $y = -1.0\,R_M$ and $y = 1.0\,R_M$ is less than $0.2\,R_M$ and is approximately symmetric. The X-lines estimated from the tailward jets (Figure 11 and Figure 8) are more than $1\,R_M$ wide in the cross-tail direction initially. As soon as the MHD-EPIC simulation starts, the duskside X-lines start to shrink (solid red lines in Figure 11 and Figure 12), so that almost all the reconnection sites are in the dawn sector at t = 30 s. The shrinkage of the X-lines may be related to the reconnection suppression region discussed by Y.-H. Liu et al. (2019).

The MESSENGER observations of current sheet thickness (Poh et al., 2017a), flux ropes, dipolarization events (Smith et al., 2017; Sun et al., 2016, 2017) and energetic electron events (Dewey et al., 2017) do not and cannot distinguish the events under different IMF conditions. For the current sheet thickness observation, the current sheet sampling is almost uniform in time. If the moderate IMF condition dominates throughout the period during which the MESSENGER observations were obtained, the asymmetric current sheet (like MHD-EPIC-A) will contribute most sampling data points in the statistics. However, strong IMF driving is likely to produce magnetotail reconnection products more frequently. Even if the moderate IMF condition occurs more frequently, it is still possible that most observed reconnection related events are produced by strong IMF drivers.

Our model assumes all the ions are protons. The heavy ions, such as sodium, have not been incorporated into the simulations. The model does not produce Kelvin-Helmholtz instability (KHI) on either side of the magnetopause. But our MHD-EPIC simulations still manifest the dawn-dusk asymmetries that are comparable with observations, which suggests that neither heavy ions nor KHI are necessary for the reconnection related dawn-dusk asymmetries, even though they may still play an important role. We have tried to incorporate sodium into our MHD model by using multispecies MHD, and therefore the sodium will also be treated as a separate ion species inside the PIC region (Ma et al., 2018). The sodium ions enter the simulation domain from the MHD inner boundary. To be specific, we set the sodium mass density to be 70% of the total mass density in the inner boundary ghost cells. This mass density matches a number density of $\sim 10\%$, which is the heavy ion abundance in the plasma sheet observe by MESSENGER (Gershman et al., 2014). The boundary condition does not introduce any dawn-dusk asymmetry by itself. This preliminary simulation shows the duskside sodium density is indeed higher than the dawnside in the current sheet (Figure 16), which is consistent with MESSEN-

GER observations. This simulation does not show any significant difference compared to the one with single ion species. Our current inner boundary condition relies on numerical diffusion to get sodium into the simulation domain from Mercury's surface and the sodium density inside the current sheet is still lower than observed by MESSENGER (Gershman et al., 2014), so we cannot draw any conclusion about the role of heavy ions so far. We will explore the role of heavy ions with an improved model in the future.

The MHD-EPIC-B simulation demonstrates that magnetic reconnection prefers the dawnside, and both MHD-EPIC-A and MHD-EPIC-B show the planetward high-speed plasma flows and dipolarization events move toward the dawnside. But it is still rare to see tailward jets beyond $y = -1.0\,R_M$ or to see planetward jets beyond $y = -0.5\,R_M$. MESSENGER observed many such events far away from the midnight direction, such as the dipolarization fronts in Figure 3 and statistics from other papers (Dewey et al., 2017; Smith et al., 2017; Sun et al., 2016). This discrepancy may be simply caused by the varying IMF in the observations. It can also be introduced by the physics that is not in our model, such as a proper heavy ion profile.

Both the MHD-EPIC and pure Hall-MHD simulations presented in this study show that the duskside current sheet is thinner than the dawnside, but the thickness obtained from Hall-MHD is significantly larger than that of MESSENGER observations and MHD-EPIC simulations. It is clear that the magnetic reconnection prefers the duakside in Hall-A simulation. There are not any significant dawn-dusk asymmetries of the reconnection products in the Hall-B simulation. In general, Hall-MHD simulations do not appear to match observations very well in terms of dawn-dusk asymmetries of magnetic reconnection. MHD-EPIC simulations contain more physics than the pure Hall-MHD simulations due to the kinetic treatment of both electrons and ions by the PIC code. This paper presents the dawn-dusk asymmetries from both the MHD-EPIC and Hall-MHD simulations and compares them with observations. A detailed comparison of the underlying physics processes in the MHD-EPIC and Hall-MHD models is outside the scope of this paper, and it can be explored in future research.

It is very difficult, if not impossible, to directly compare the numerical diffusion in the Hall MHD and PIC, since they are solving different equations. To make a fair comparison, we use similar grid resolutions (section 2) in the tail region for both MHD and PIC. Figure 1(b) and (d) show the Hall magnetic field B_y from the MHD-EPIC-A and

Hall-A simulations, respectively. Both plots show B_y of similar amplitude, which suggests that the difference in the numerical diffusion of the MHD-EPIC simulations and the Hall-MHD simulations is not significant.

The dayside magnetopause is not covered by the PIC code in the present study due to the small kinetic scales in the magnetosheath. The magnetosheath ion density is about 100 amu/cc and the corresponding ion inertial length is just about 20 km or $1/120 R_M$. It is extremely difficult to resolve such small scales with a PIC code. Even though the present simulations incorporate the Hall term into the fluid model, the grid is not fine enough to well resolve the Hall effect near the dayside magnetopause, and BATS-R-US degenerates to an ideal MHD model in this case. The present simulations do not introduce significant dawn-dusk asymmetries through the dayside magnetopause. However, the dayside magnetopause may produce asymmetries in reality due to the gyro-motion of particles and the separation of electrons and ions. We are studying Mercury's dayside magnetopause with a refined grid now, and the results will be reported in future papers.

6 Summary

We use the MHD-EPIC model to study dawn-dusk asymmetries of Mercury's magnetotail. The simulation results, such as the current sheet thickness, plasma density asymmetry, and reconnection asymmetry, agree with MESSENGER observations. The key simulation results are:

- The dawnside plasma density and electron pressure are higher than the duskside. The proton pressure does not exhibit significant dawn-dusk asymmetry in the simulations.
- The dawnside current sheet is thicker than the duskside.
- When the IMF driver is moderate, for example, $B_z = -8.5\,nT$, the current sheet thickness asymmetry is strong, and the magnetotail X-lines may prefer the duskside. When the IMF driver is strong, for example, $B_z = -19.4\,nT$, the current sheet thickness asymmetry is not significant, and the magnetotail reconnection prefers the dawnside.
- The dipolarization events and the planetward high-speed plasma flows, including both proton flows and electron flows, concentrate in the dawn sector.

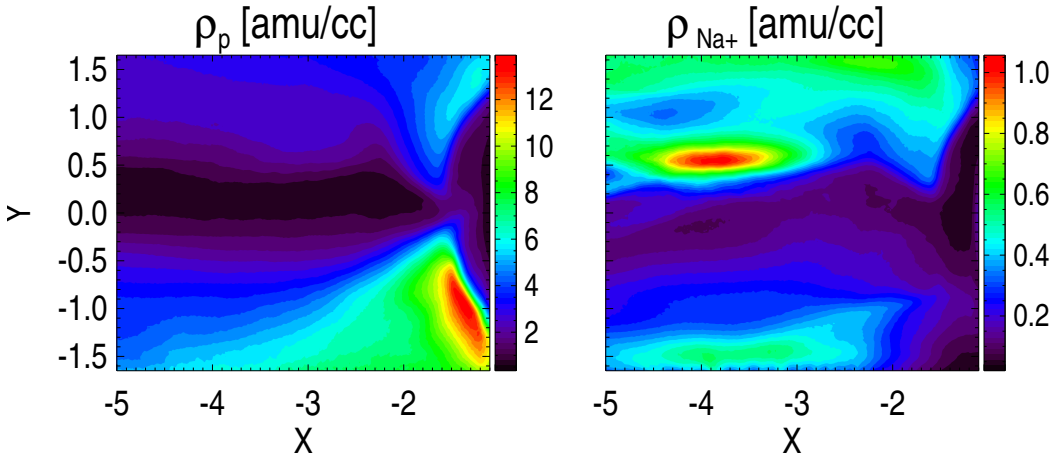

Figure 16. The proton and sodium density on the current sheet surface for multispecies-MHD-EPIC.

- The preliminary multispecies-MHD-EPIC simulation produces higher duskside sodium density in the current sheet but does not change the asymmetry of the reconnection significantly.

Acknowledgments

This work was supported by the INSPIRE NSF grant PHY-1513379, the NSF PREEVENTS grant 1663800, the Impacts of Extreme Space Weather Events on Power Grid Infrastructure project funded by the U.S. Department of Energy (DE-AC52-06NA25396) through the Los Alamos National Laboratory Directed Research and Development program, the NASA Living With a Star program grant NNX16AJ67G and the NASA's Solar System-Workings program grant NNX15AH28G. Computational resources supporting this work were provided on the Blue Waters super computer by the NSF PRAC grant ACI-1640510, on the Pleiades computer by NASA High-End Computing (HEC) Program through the NASA Advanced Supercomputing (NAS) Division at Ames Research Center, and from Cheyenne (doi:10.5065/D6RX99HX) provided by NCAR's Computational and Information Systems Laboratory, sponsored by the National Science Foundation.

MESSENGER data used in this study were available from the Planetary Data System (PDS): http://pds.jpl.nasa.gov. The MESSENGER project is supported by the NASA Discovery Program under contracts NASW-00002 to the Carnegie Institution of Washington and NAS5-97271 to The Johns Hopkins University Applied Physics Laboratory.

The SWMF code (including BATS-R-US and iPIC3D) is publicly available through the csem.engin.umich.edu/tools/swmf web site after registration. The output of the simulations presented in this paper can be obtained through the shared endpoint 'Chen_2019_Mercury_SWMF_data' on Globus (https://www.globus.org/).

References

Anderson, B. J., Acuña, M. H., Lohr, D. A., Scheifele, J., Raval, A., Korth, H., & Slavin, J. A. (2007). The magnetometer instrument on MESSENGER. *Space Science Reviews*, *131*(1), 417–450. doi: 10.1007/s11214-007-9246-7

Anderson, B. J., Johnson, C. L., Korth, H., Purucker, M. E., Winslow, R. M., Slavin, J. A., ... Zurbuchen, T. H. (2011). The global magnetic field of Mercury from MESSENGER orbital observations. *Science*, *333*(6051), 1859–1862. doi: 10.1126/science.1211001

Andrews, G. B., Zurbuchen, T. H., Mauk, B. H., Malcom, H., Fisk, L. A., Gloeckler, G., ... Raines, J. M. (2007). The energetic particle and plasma spectrometer instrument on the MESSENGER spacecraft. *Space Science Reviews*, *131*(1), 523–556. doi: 10.1007/s11214-007-9272-5

Angelopoulos, V., Runov, A., Zhou, X.-Z., Turner, D. L., Kiehas, S. A., Li, S.-S., & Shinohara, I. (2013). Electromagnetic energy conversion at reconnection fronts. *Science*, *341*(6153), 1478–1482. doi: 10.1126/science.1236992

Baker, D. N., Dewey, R. M., Lawrence, D. J., Goldsten, J. O., Peplowski, P. N., Korth, H., ... Solomon, S. C. (2016). Intense energetic electron flux enhancements in Mercury's magnetosphere: An integrated view with high-resolution observations from MESSENGER. *J. Geophys. Res.*, *121*(3), 2171-2184. doi: 10.1002/2015JA021778

Benna, M., Anderson, B. J., Baker, D. N., Boardsen, S. A., Gloeckler, G., Gold, R. E., ... Zurbuchen, T. H. (2010). Modeling of the magnetosphere of Mercury at the time of the first MESSENGER flyby. *Icarus*, *209*(1), 3–10. doi: https://doi.org/10.1016/j.icarus.2009.11.036

Chen, Y., & Tóth, G. (2019). Gauss's law satisfying energy-conserving semi-implicit particle-in-cell method. *J. Comput. Phys.*, *386*, 632. doi: 10.1016/j.jcp.2019.02.032

Chen, Y., Tóth, G., Cassak, P., Jia, X., Gombosi, T. I., Slavin, J., ... Peng, B. (2017). Global three-dimensional simulation of Earth's dayside reconnection using a two-way coupled magnetohydrodynamics with embedded particle-in-cell model: Initial results. *J. Geophys. Res.*, *122*, 10318. doi: 10.1002/2017JA024186

Daldorff, L. K. S., Tóth, G., Gombosi, T. I., Lapenta, G., Amaya, J., Markidis, S., &

Brackbill, J. U. (2014). Two-way coupling of a global Hall magnetohydrodynamics model with a local implicit Particle-in-Cell model. *J. Comput. Phys.*, *268*, 236. doi: 10.1016/j.jcp.2014.03.009

Delcourt, D. (2013). On the supply of heavy planetary material to the magnetotail of Mercury. *Annales Geophysicae*, *31*(10), 1673–1679. doi: 10.5194/angeo-31-1673-2013

Delcourt, D. C., Grimald, S., Leblanc, F., Berthelier, J.-J., Millilo, A., Mura, A., ... Moore, T. (2003). A quantitative model of the planetary Na+ contribution to Mercury's magnetosphere. *Annales Geophysicae*, *21*(8), 1723–1736. doi: 10.5194/angeo-21-1723-2003

Dewey, R. M., Raines, J. M., Sun, W., Slavin, J. A., & Poh, G. (2018). MESSENGER observations of fast plasma flows in Mercury's magnetotail. *Geophys. Res. Lett.*, *45*(19), 10,110-10,118. doi: 10.1029/2018GL079056

Dewey, R. M., Slavin, J. A., Raines, J. M., Baker, D. N., & Lawrence, D. J. (2017). Energetic electron acceleration and injection during dipolarization events in Mercury's magnetotail. *J. Geophys. Res.*, *122*(12), 12,170-12,188. doi: 10.1002/2017JA024617

DiBraccio, G. A., Slavin, J. A., Imber, S. M., Gershman, D. J., Raines, J. M., Jackman, C. M., ... others (2015). MESSENGER observations of flux ropes in Mercury's magnetotail. *Planetary and Space Science*, *115*, 77–89. doi: https://doi.org/10.1016/j.pss.2014.12.016

Dorelli, J. C., Glocer, A., Collinson, G., & Toth, G. (2015). The role of the Hall effect in the global structure and dynamics of planetary magnetospheres: Ganymede as a case study. *J. Geophys. Res.*, *120*, 5377–5392. doi: 10.1002/2014JA020951

Gershman, D. J., Slavin, J. A., Raines, J. M., Zurbuchen, T. H., Anderson, B. J., Korth, H., ... Solomon, S. C. (2013). Magnetic flux pileup and plasma depletion in Mercury's subsolar magnetosheath. *J. Geophys. Res.*, *118*(11), 7181-7199. doi: 10.1002/2013JA019244

Gershman, D. J., Slavin, J. A., Raines, J. M., Zurbuchen, T. H., Anderson, B. J., Korth, H., ... Solomon, S. C. (2014). Ion kinetic properties in Mercury's pre-midnight plasma sheet. *Geophys. Res. Lett.*, *41*(16), 5740-5747. doi: 10.1002/2014GL060468

Ho, G. C., Starr, R. D., Krimigis, S. M., Vandegriff, J. D., Baker, D. N., Gold, R. E., ... Solomon, S. C. (2016). MESSENGER observations of suprathermal electrons in Mercury's magnetosphere. *Geophys. Res. Lett.*, *43*(2), 550-555. doi: 10.1002/2015GL066850

Imber, S. M., Slavin, J. A., Auster, H. U., & Angelopoulos, V. (2011). A THEMIS survey of flux ropes and traveling compression regions: Location of the near-Earth reconnection site during solar minimum. *J. Geophys. Res.*, *116*(A2). doi: 10.1029/2010JA016026

Jia, X., Slavin, J. A., Gombosi, T. I., Daldorff, L. K. S., Toth, G., & van der Holst, B. (2015). Global MHD simulations of Mercury's magnetosphere with coupled planetary interior: Induction effect of the planetary conducting core on the global interaction. *J. Geophys. Res.*, *120*(6), 4763–4775. doi: 10.1002/2015JA021143

Jia, X., Slavin, J. A., Poh, G., DiBraccio, G. A., Toth, G., Chen, Y., ... Gombosi, T. I. (2019). MESSENGER observations and global simulations of highly compressed magnetosphere events at Mercury. *J. Geophys. Res.*, *124*(1), 229-247. doi: 10.1029/2018JA026166

Kabin, K., Gombosi, T. I., De Zeeuw, D. L., & Powell, K. G. (2000). Interaction of Mercury with the solar wind. *Icarus*, *143*, 397–406. doi: https://doi.org/10.1006/icar.1999.6252

Kabin, K., Heimpel, M., Rankin, R., Aurnou, J., Gómez-Pérez, N., Paral, J., ... DeZeeuw, D. (2008). Global MHD modeling of Mercury's magnetosphere with applications to the MESSENGER mission and dynamo theory. *Icarus*, *195*(1), 1 - 15. doi: http://dx.doi.org/10.1016/j.icarus.2007.11.028

Kallio, E., & Janhunen, P. (2003). Modelling the solar wind interaction with Mercury by a quasi-neutral hybrid model. *Annales Geophysicae*, *21*(11), 2133–2145. doi: 10.5194/angeo-21-2133-2003

Kidder, A., Winglee, R., & Harnett, E. (2008). Erosion of the dayside magnetosphere at Mercury in association with ion outflows and flux rope generation. *J. Geophys. Res.*, *113*(A9). doi: 10.1029/2008JA013038

Korth, H., Anderson, B. J., Gershman, D. J., Raines, J. M., Slavin, J. A., Zurbuchen, T. H., ... McNutt Jr., R. L. (2014). Plasma distribution in Mercury's magnetosphere derived from MESSENGER Magnetometer and Fast Imaging

Plasma Spectrometer observations. *J. Geophys. Res.*, *119*(4), 2917-2932. doi: 10.1002/2013JA019567

Lapenta, G. (2017). Exactly energy conserving semi-implicit particle in cell formulation. *J. Comput. Phys.*, *334*, 349–366. doi: https://doi.org/10.1016/j.jcp.2017.01.002

Lin, Y., Wang, X. Y., Lu, S., Perez, J. D., & Lu, Q. (2014). Investigation of storm time magnetotail and ion injection using three-dimensional global hybrid simulation. *J. Geophys. Res.*, *119*(9), 7413-7432. doi: 10.1002/2014JA020005

Lindsay, S., James, M., Bunce, E., Imber, S., Korth, H., Martindale, A., & Yeoman, T. (2016). MESSENGER X-ray observations of magnetosphere-surface interaction on the nightside of Mercury. *Planetary and Space Science*, *125*, 72 - 79. doi: https://doi.org/10.1016/j.pss.2016.03.005

Liu, J., Angelopoulos, V., Runov, A., & Zhou, X.-Z. (2013). On the current sheets surrounding dipolarizing flux bundles in the magnetotail: The case for wedgelets. *J. Geophys. Res.*, *118*(5), 2000-2020. doi: 10.1002/jgra.50092

Liu, Y.-H., Li, T. C., Hesse, M., Sun, W. J., Liu, J., Burch, J., ... Huang, K. (2019). 3D magnetic reconnection with a spatially confined X-line extent – implications for dipolarizing flux bundles and the dawn-dusk asymmetry. *J. Geophys. Res.*, *0*(ja). doi: 10.1029/2019JA026539

Lu, S., Artemyev, A., Angelopoulos, V., Lin, Y., Zhang, X.-J., Liu, J., ... Strangeway, R. (2019). The Hall electric field in Earth's magnetotail thin current sheet. *J. Geophys. Res.*, *124*(2), 1052–1062. doi: 10.1029/2018JA026202

Lu, S., Lin, Y., Angelopoulos, V., Artemyev, A., Pritchett, P., Lu, Q., & Wang, X. (2016). Hall effect control of magnetotail dawn-dusk asymmetry: A three-dimensional global hybrid simulation. *J. Geophys. Res.*. doi: 10.1002/2016JA023325

Lu, S., Pritchett, P. L., Angelopoulos, V., & Artemyev, A. V. (2018). Formation of dawn-dusk asymmetry in Earth's magnetotail thin current sheet: A three-dimensional particle-in-cell simulation. *J. Geophys. Res.*, *123*(4), 2801-2814. doi: 10.1002/2017JA025095

Ma, Y., Russell, C. T., Toth, G., Chen, Y., Nagy, A. F., Harada, Y., ... Jakosky, B. M. (2018). Reconnection in the Martian magnetotail: Hall-MHD with embedded particle-in-cell simulations. *J. Geophys. Res.*, *123*(5), 3742-3763. doi:

10.1029/2017JA024729

Markidis, S., Lapenta, G., & Rizwan-Uddin. (2010). Multi-scale simulations of plasma with iPIC3D. *Mathematics and Computers in Simulation*, *80*, 1509–1519. doi: 10.1016/j.matcom.2009.08.038

Müller, J., Simon, S., Wang, Y.-C., Motschmann, U., Heyner, D., Schüle, J., ... Pringle, G. J. (2012). Origin of Mercury's double magnetopause: 3D hybrid simulation study with AIKEF. *Icarus*, *218*(1), 666–687. doi: https://doi.org/10.1016/j.icarus.2011.12.028

Poh, G., Slavin, J. A., Jia, X., Raines, J. M., Imber, S. M., Sun, W.-J., ... Smith, A. W. (2017a). Coupling between Mercury and its nightside magnetosphere: Cross-tail current sheet asymmetry and substorm current wedge formation. *J. Geophys. Res.*, *122*(8), 8419–8433. doi: 10.1002/2017JA024266

Poh, G., Slavin, J. A., Jia, X., Raines, J. M., Imber, S. M., Sun, W.-J., ... Smith, A. W. (2017b). Mercury's cross-tail current sheet: Structure, X-line location and stress balance. *Geophys. Res. Lett.*, *44*(2), 678–686. doi: 10.1002/2016GL071612

Poh, G., Slavin, J. A., Jia, X., Sun, W.-J., Raines, J. M., Imber, S. M., ... Gershman, D. J. (2018). Transport of mass and energy in Mercury's plasma sheet. *Geophys. Res. Lett.*, *45*(22), 12,163-12,170. doi: 10.1029/2018GL080601

Powell, K., Roe, P., Linde, T., Gombosi, T., & De Zeeuw, D. L. (1999). A solution-adaptive upwind scheme for ideal magnetohydrodynamics. *J. Comput. Phys.*, *154*, 284-309. doi: 10.1006/jcph.1999.6299

Raines, J. M., Gershman, D. J., Zurbuchen, T. H., Sarantos, M., Slavin, J. A., Gilbert, J. A., ... Solomon, S. C. (2013). Distribution and compositional variations of plasma ions in Mercury's space environment: The first three Mercury years of MESSENGER observations. *J. Geophys. Res.*, *118*(4), 1604-1619. doi: 10.1029/2012JA018073

Raines, J. M., Slavin, J. A., Zurbuchen, T. H., Gloeckler, G., Anderson, B. J., Baker, D. N., ... McNutt, R. L. (2011). MESSENGER observations of the plasma environment near Mercury. *Planetary and Space Science*, *59*(15), 2004 - 2015. doi: https://doi.org/10.1016/j.pss.2011.02.004

Schriver, D., Travnicek, P. M., Lapenta, G., Amaya, J., Gonzalez, D., Richard, R., ... Hellinger, P. (2017). Global particle-in-cell simulations of Mercury's

magnetosphere. In *Agu fall meeting abstracts.*

Schriver, D., Trávníček, P., Ashour-Abdalla, M., Richard, R. L., Hellinger, P., Slavin, J. A., ... Starr, R. D. (2011). Electron transport and precipitation at Mercury during the MESSENGER flybys: Implications for electron-stimulated desorption. *Planetary and Space Science*, *59*(15), 2026 - 2036. doi: https://doi.org/10.1016/j.pss.2011.03.008

Seki, K., Terada, N., Yagi, M., Delcourt, D., Leblanc, F., & Ogino, T. (2013). Effects of the surface conductivity and the IMF strength on the dynamics of planetary ions in Mercury's magnetosphere. *J. Geophys. Res.*, *118*(6), 3233-3242. doi: 10.1002/jgra.50181

Slavin, J. A., Acuña, M. H., Anderson, B. J., Baker, D. N., Benna, M., Boardsen, S. A., ... others (2009). MESSENGER observations of magnetic reconnection in Mercury's magnetosphere. *Science*, *324*(5927), 606–610. doi: 10.1126/science.1172011

Slavin, J. A., Anderson, B. J., Baker, D. N., Benna, M., Boardsen, S. A., Gloeckler, G., ... others (2010). MESSENGER observations of extreme loading and unloading of Mercury's magnetic tail. *Science*, *329*(5992), 665–668. doi: 10.1126/science.1188067

Slavin, J. A., Anderson, B. J., Baker, D. N., Benna, M., Boardsen, S. A., Gold, R. E., ... others (2012). MESSENGER and Mariner 10 flyby observations of magnetotail structure and dynamics at Mercury. *J. Geophys. Res.*, *117*(A1). doi: 10.1029/2011JA016900

Slavin, J. A., Imber, S. M., Boardsen, S. A., DiBraccio, G. A., Sundberg, T., Sarantos, M., ... Solomon, S. C. (2012). MESSENGER observations of a flux-transfer-event shower at Mercury. *J. Geophys. Res.*, *117*(A12). doi: 10.1029/2012JA017926

Smith, A. W., Slavin, J. A., Jackman, C. M., Poh, G.-K., & Fear, R. C. (2017). Flux ropes in the Hermean magnetotail: Distribution, properties, and formation. *J. Geophys. Res.*, *122*(8), 8136-8153. doi: 10.1002/2017JA024295

Solomon, S. C., McNutt, R. L., Gold, R. E., & Domingue, D. L. (2007). MESSENGER mission overview. *Space Science Reviews*, *131*(1), 3–39. doi: 10.1007/s11214-007-9247-6

Sun, W. J., Fu, S., Slavin, J., Raines, J., Zong, Q., Poh, G., & Zurbuchen, T.

(2016). Spatial distribution of Mercury's flux ropes and reconnection fronts: MESSENGER observations. *J. Geophys. Res.*, *121*(8), 7590–7607. doi: 10.1002/2016JA022787

Sun, W. J., Raines, J. M., Fu, S. Y., Slavin, J. A., Wei, Y., Poh, G. K., ... Wan, W. X. (2017). MESSENGER observations of the energization and heating of protons in the near-Mercury magnetotail. *Geophys. Res. Lett.*, *44*(16), 8149–8158. doi: 10.1002/2017GL074276

Sun, W. J., Slavin, J. A., Dewey, R. M., Raines, J. M., Fu, S. Y., Wei, Y., ... Zhao, D. (2018). A comparative study of the proton properties of magnetospheric substorms at Earth and Mercury in the near magnetotail. *Geophys. Res. Lett.*, *45*(16), 7933-7941. doi: 10.1029/2018GL079181

Sun, W.-J., Slavin, J. A., Fu, S., Raines, J. M., Zong, Q.-G., Imber, S. M., ... Baker, D. N. (2015). MESSENGER observations of magnetospheric substorm activity in Mercury's near magnetotail. *Geophys. Res. Lett.*, *42*(10), 3692-3699. doi: 10.1002/2015GL064052

Tóth, G., Chen, Y., Gombosi, T. I., Cassak, P., Markidis, S., & Peng, I. B. (2017). Scaling the ion inertial length and its implications for modeling reconnection in global simulations. *J. Geophys. Res.*, *122*(10). doi: 10.1002/2017JA024189

Tóth, G., Jia, X., Markidis, S., Peng, B., Chen, Y., Daldorff, L., ... Dorelli, J. (2016). Extended magnetohydrodynamics with embedded particle-in-cell simulation of Ganymede's magnetosphere. *J. Geophys. Res.*, *121*. doi: 10.1002/2015JA021997

Tóth, G., Ma, Y. J., & Gombosi, T. I. (2008). Hall magnetohydrodynamics on block adaptive grids. *J. Comput. Phys.*, *227*, 6967-6984. doi: 10.1016/j.jcp.2008.04.010

Tóth, G., Sokolov, I. V., Gombosi, T. I., Chesney, D. R., Clauer, C., Zeeuw, D. L. D., ... Kóta, J. (2005). Space Weather Modeling Framework: A new tool for the space science community. *J. Geophys. Res.*, *110*, A12226. doi: 10.1029/2005JA011126

Tóth, G., van der Holst, B., Sokolov, I. V., Zeeuw, D. L. D., Gombosi, T. I., Fang, F., ... Opher, M. (2012). Adaptive numerical algorithms in space weather modeling. *J. Comput. Phys.*, *231*, 870–903. doi: 10.1016/j.jcp.2011.02.006

Travnicek, P. M., Schriver, D., Hellinger, P., Herčík, D., Anderson, B. J., Saran-

tos, M., & Slavin, J. A. (2010). Mercury's magnetosphere–solar wind interaction for northward and southward interplanetary magnetic field: Hybrid simulation results. *Icarus*, *209*(1), 11 - 22. doi: https://doi.org/10.1016/j.icarus.2010.01.008

Wang, Y.-C., Mueller, J., Motschmann, U., & Ip, W.-H. (2010). A hybrid simulation of Mercury's magnetosphere for the MESSENGER encounters in year 2008. *Icarus*, *209*(1), 46–52. doi: https://doi.org/10.1016/j.icarus.2010.05.020

Winslow, R. M., Anderson, B. J., Johnson, C. L., Slavin, J. A., Korth, H., Purucker, M. E., ... Solomon, S. C. (2013). Mercury's magnetopause and bow shock from MESSENGER Magnetometer observations. *J. Geophys. Res.*, *118*(5), 2213–2227. doi: 10.1002/jgra.50237

Zhou, H., Toth, G., Jia, X., Chen, Y., & Markidis, S. (2019). Embedded kinetic simulation of Ganymede's magnetosphere: Improvements and inferences. *J. Geophys. Res.*, *0*(0). doi: 10.1029/2019JA026643

Zhou, X.-Z., Angelopoulos, V., Sergeev, V. A., & Runov, A. (2010). Accelerated ions ahead of earthward propagating dipolarization fronts. *J. Geophys. Res.*, *115*(A5). doi: 10.1029/2010JA015481

cartoon.

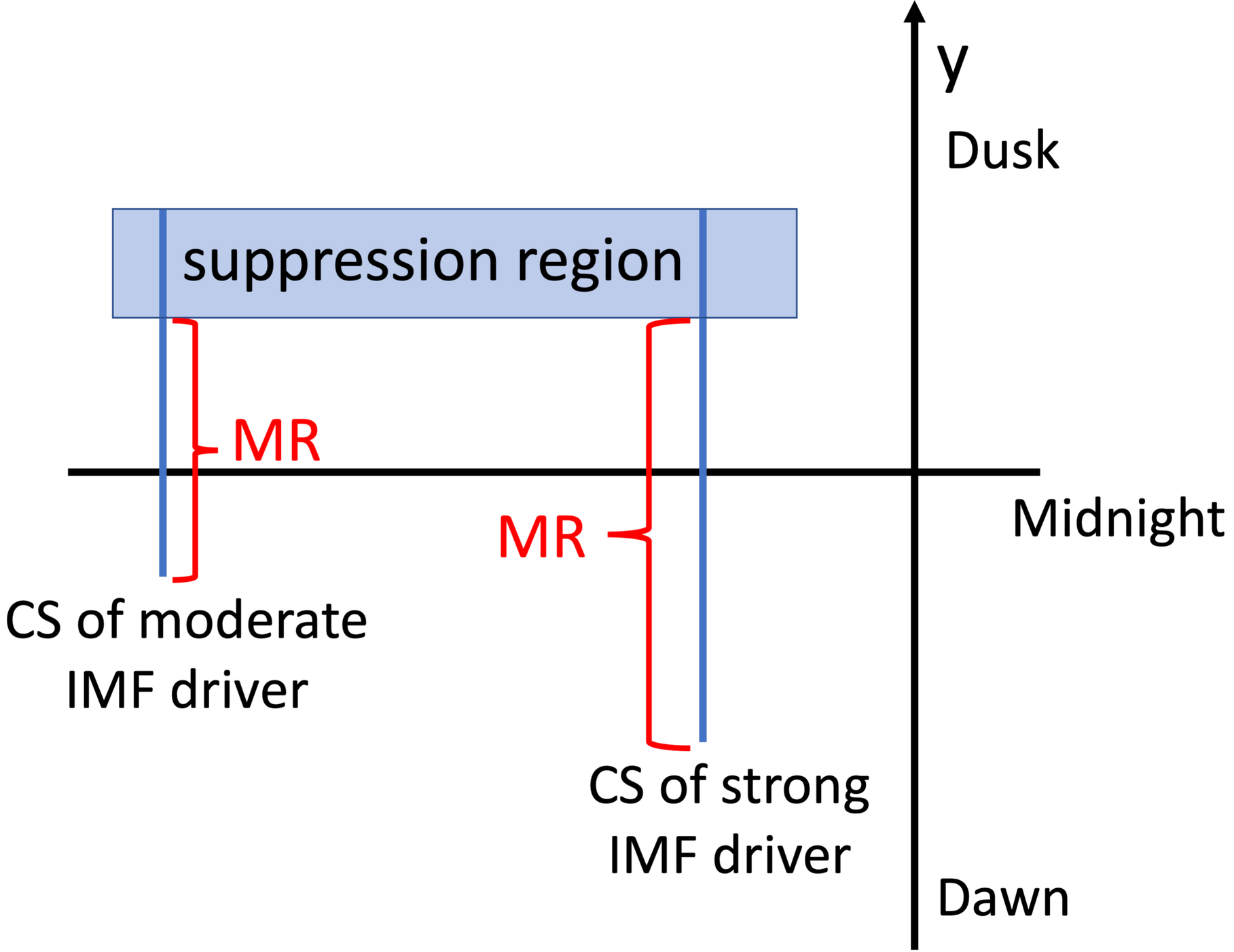

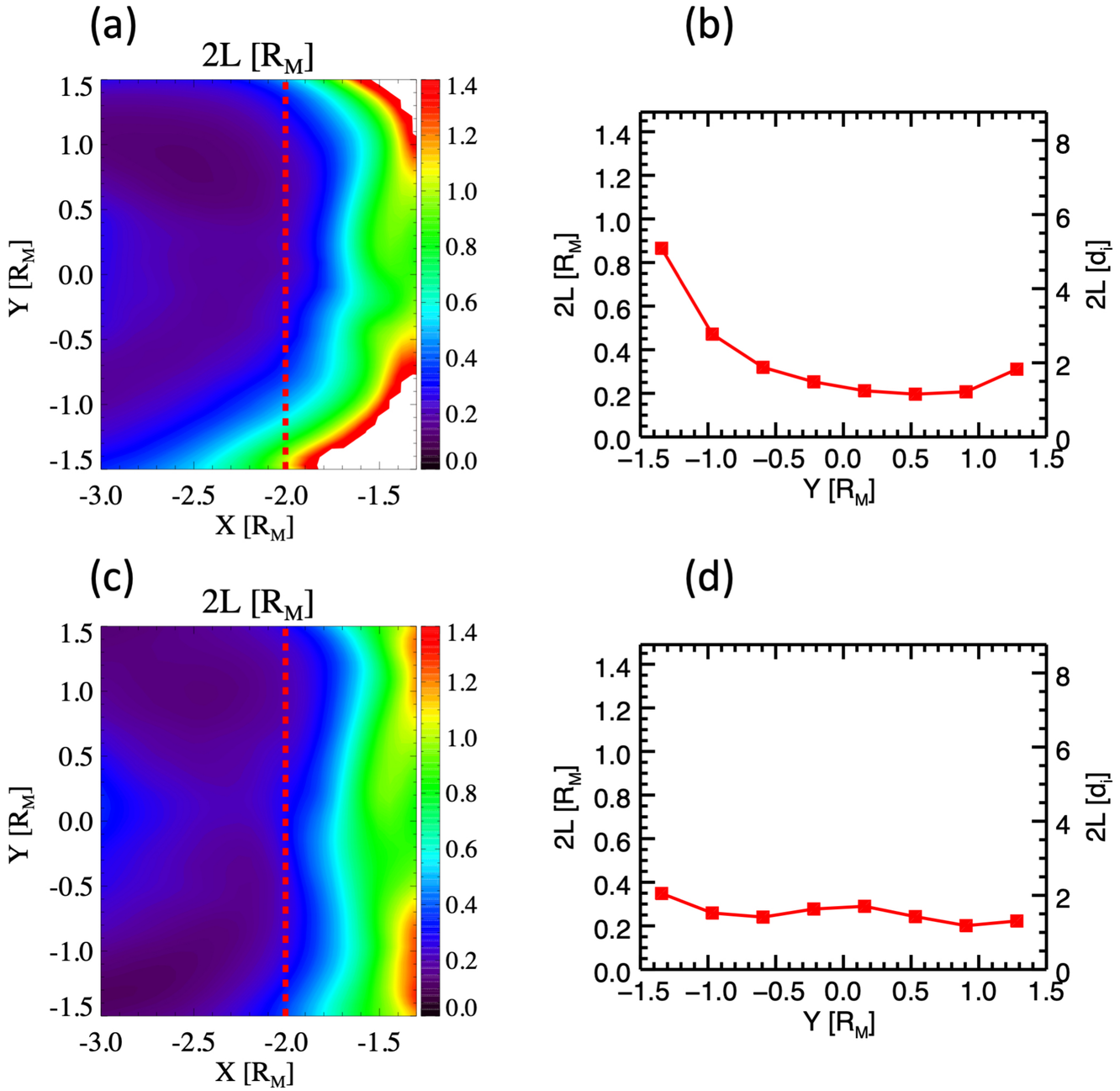

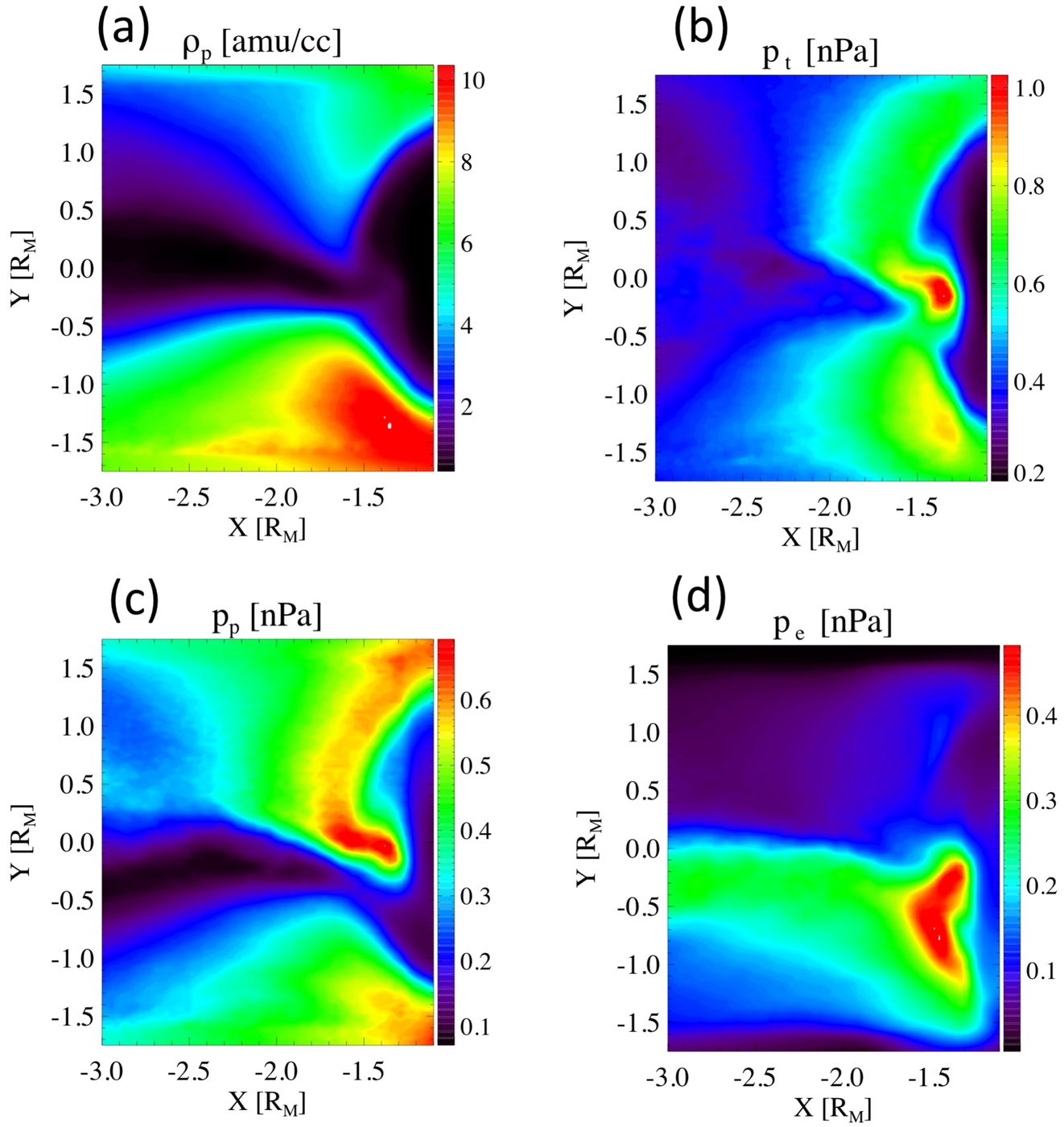

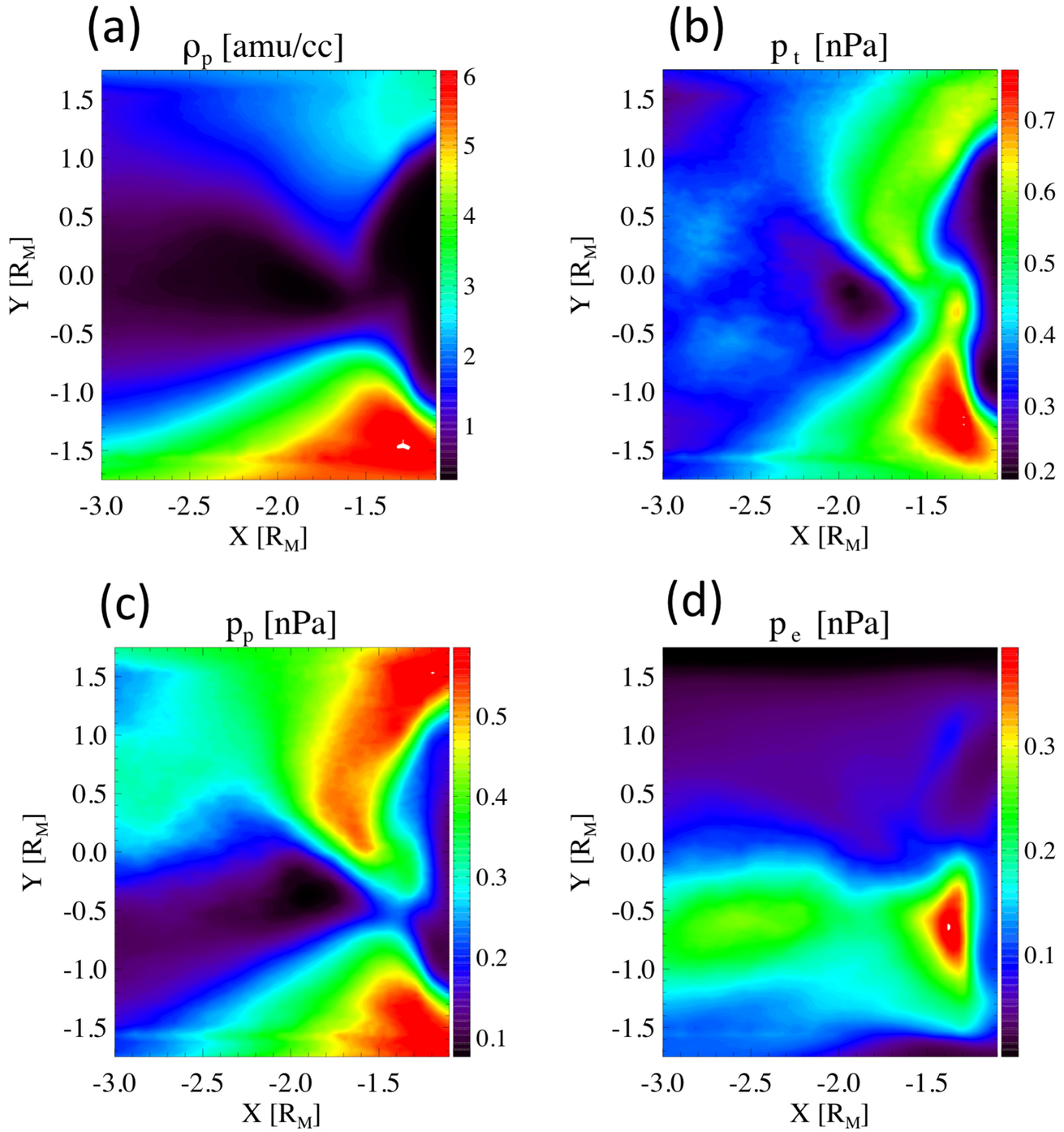

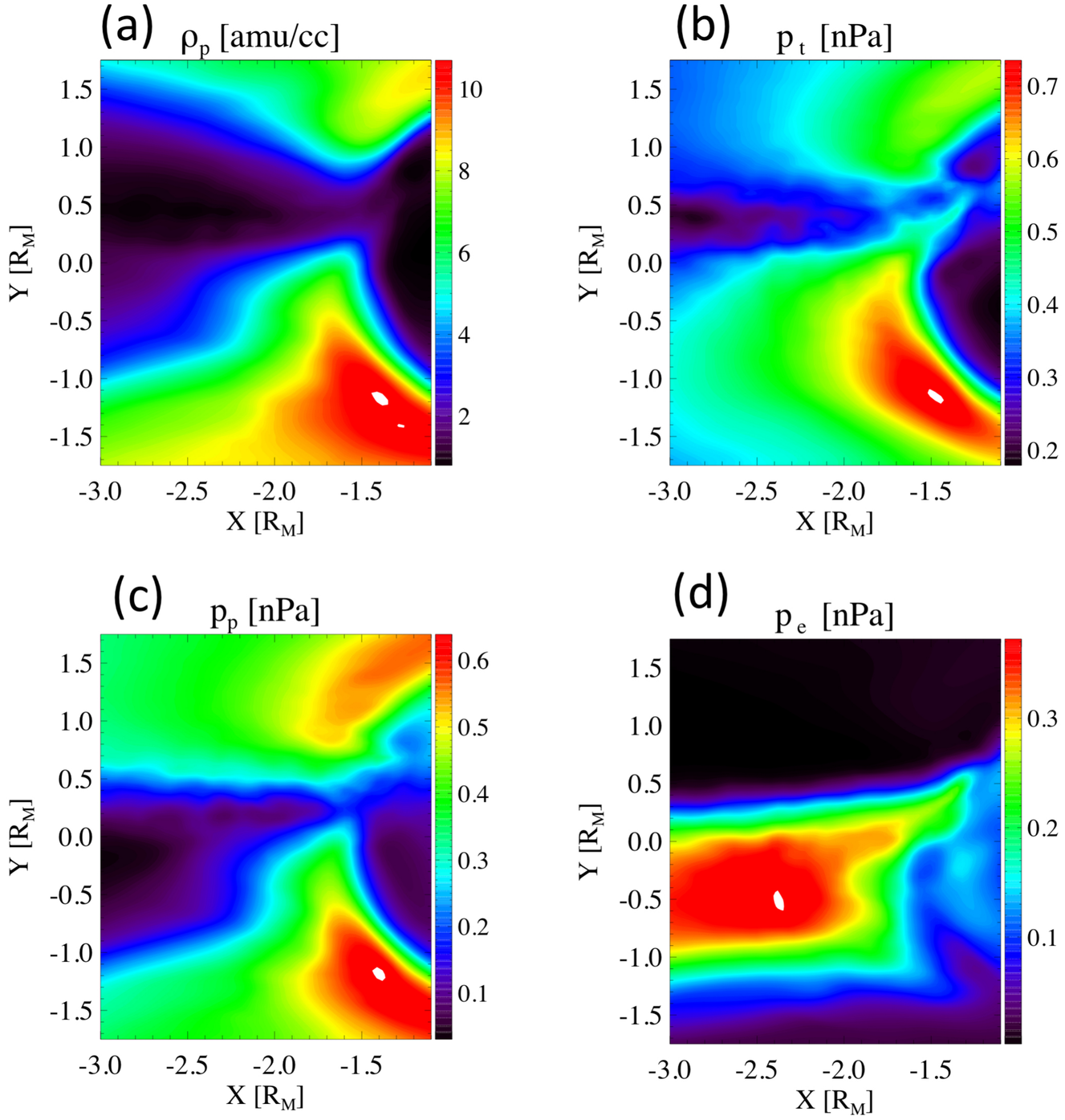

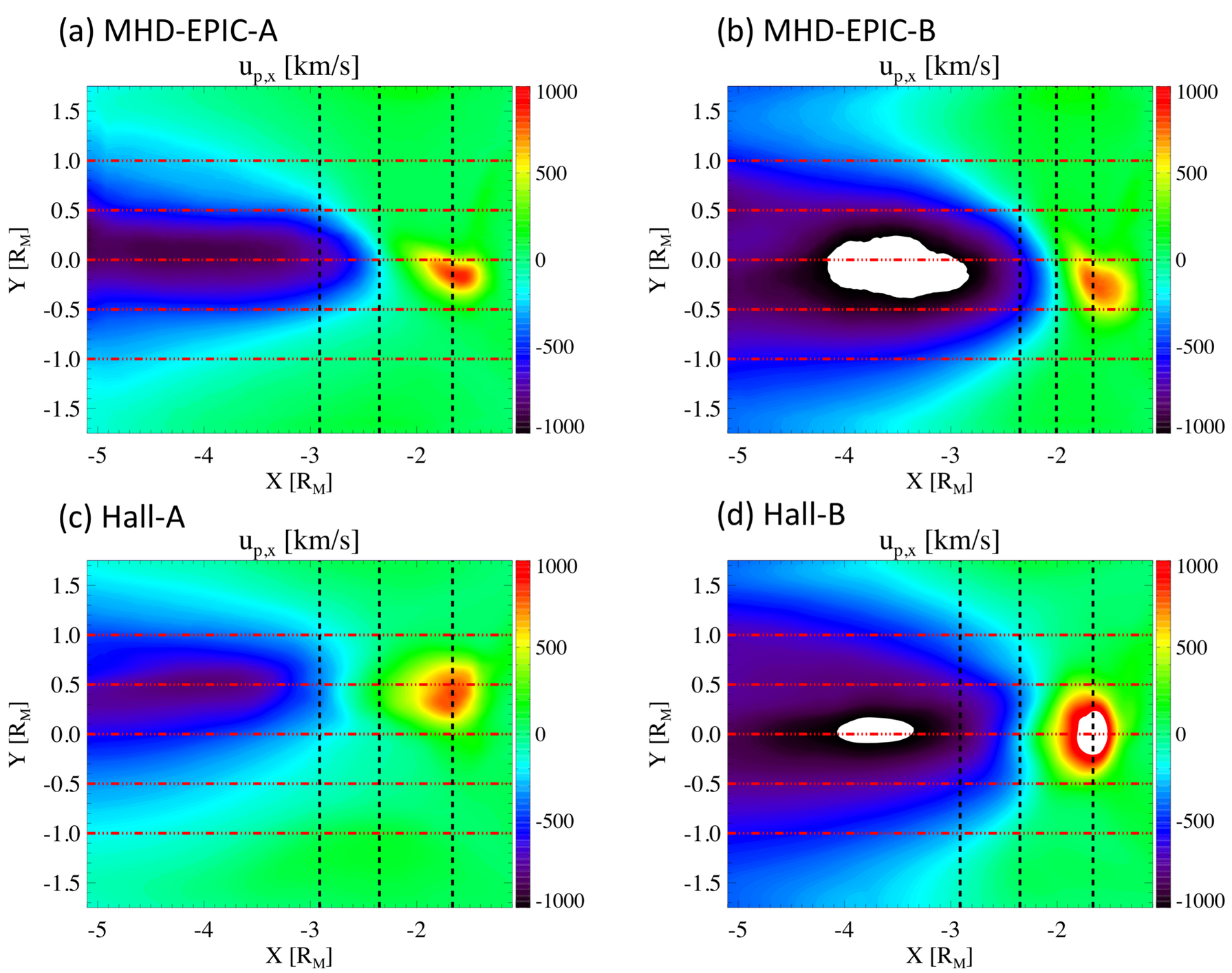

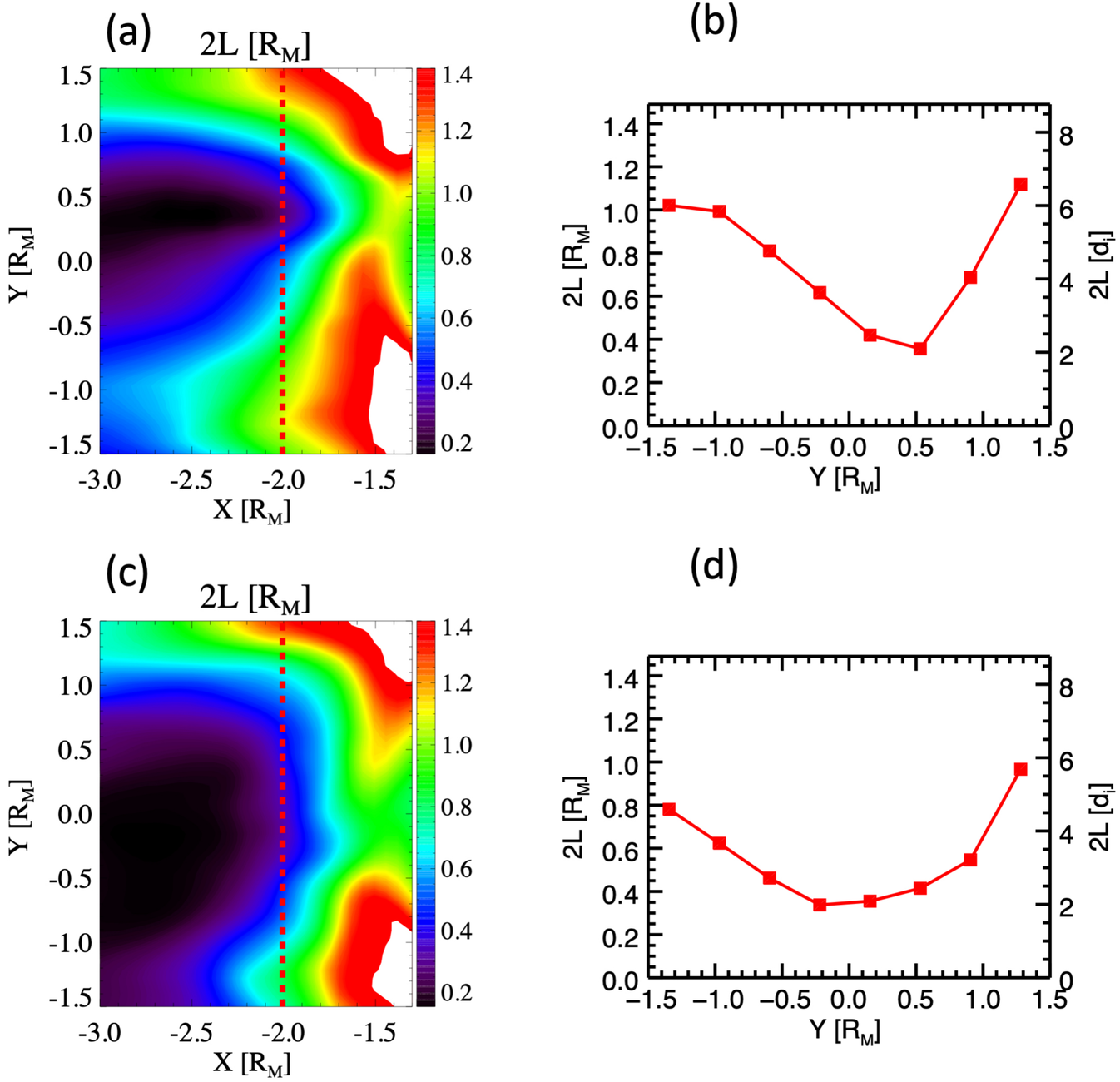

comb_df.

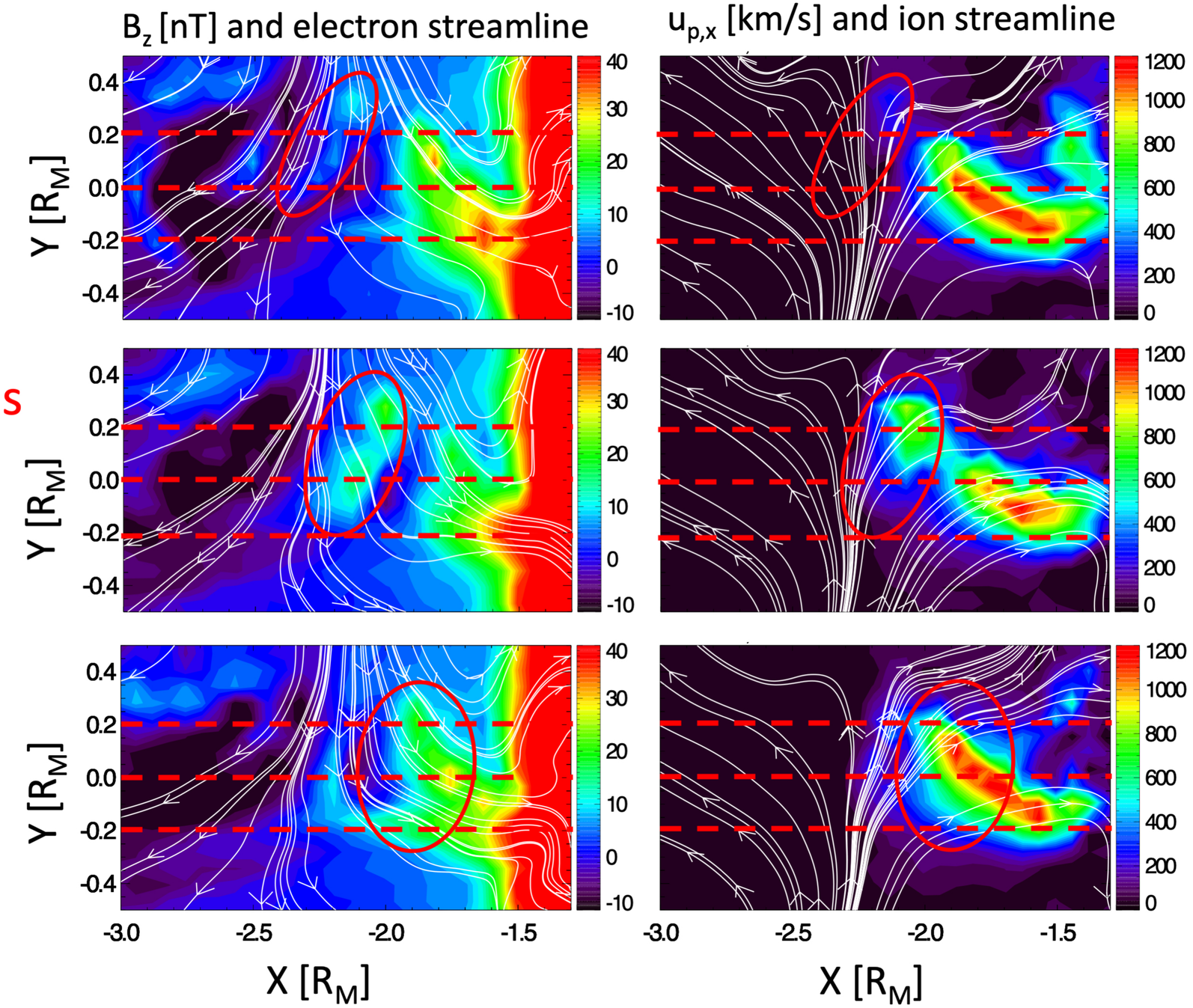

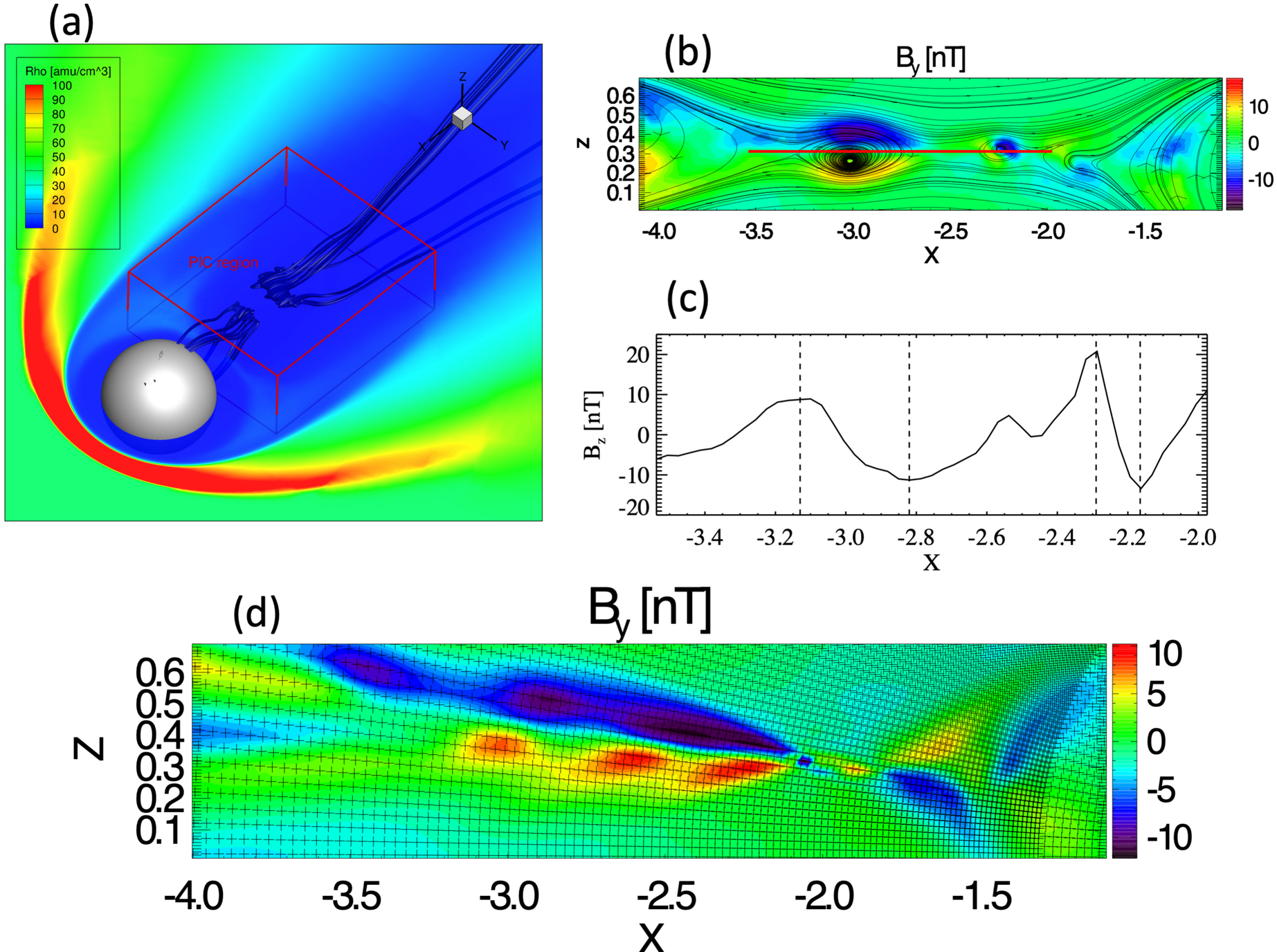

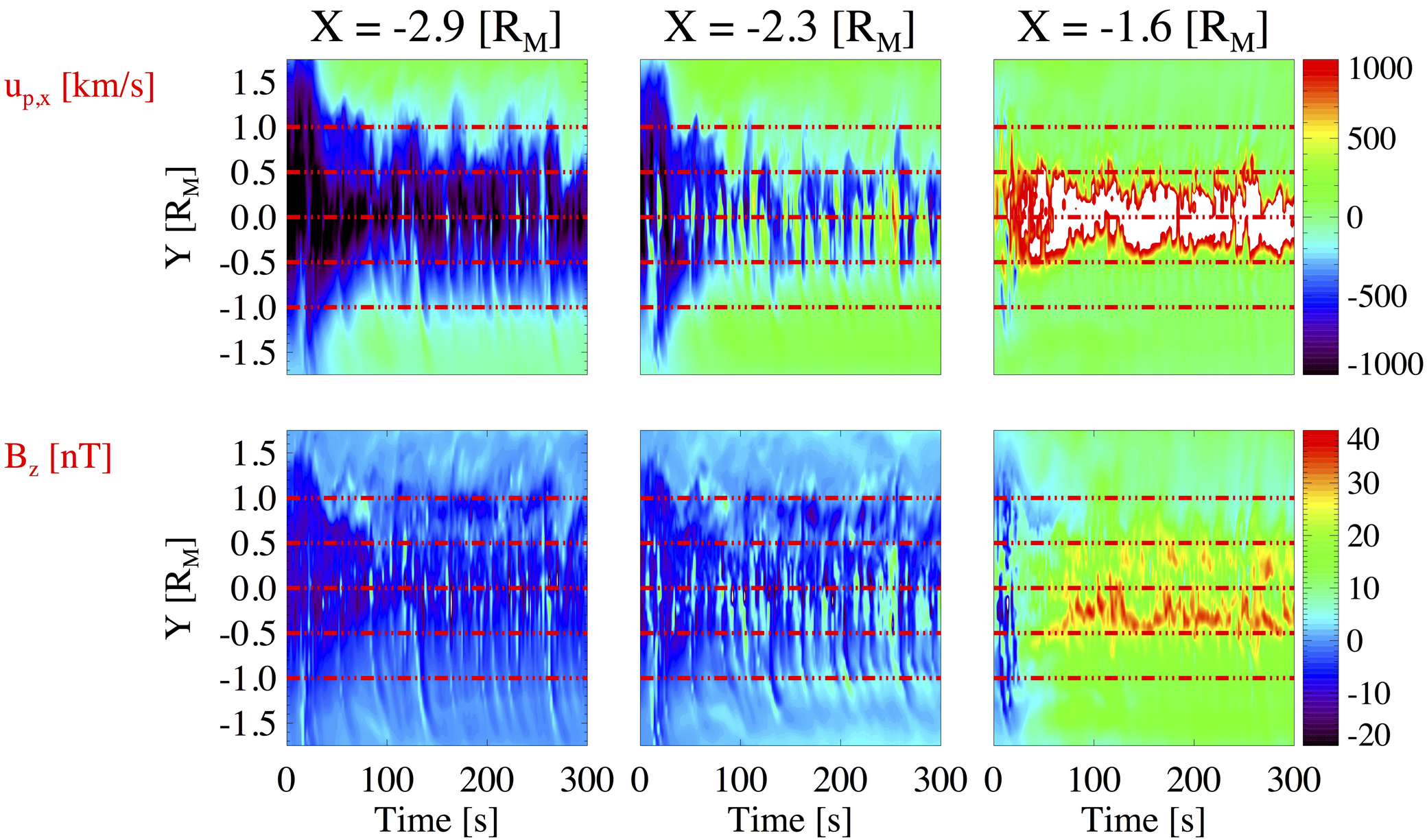

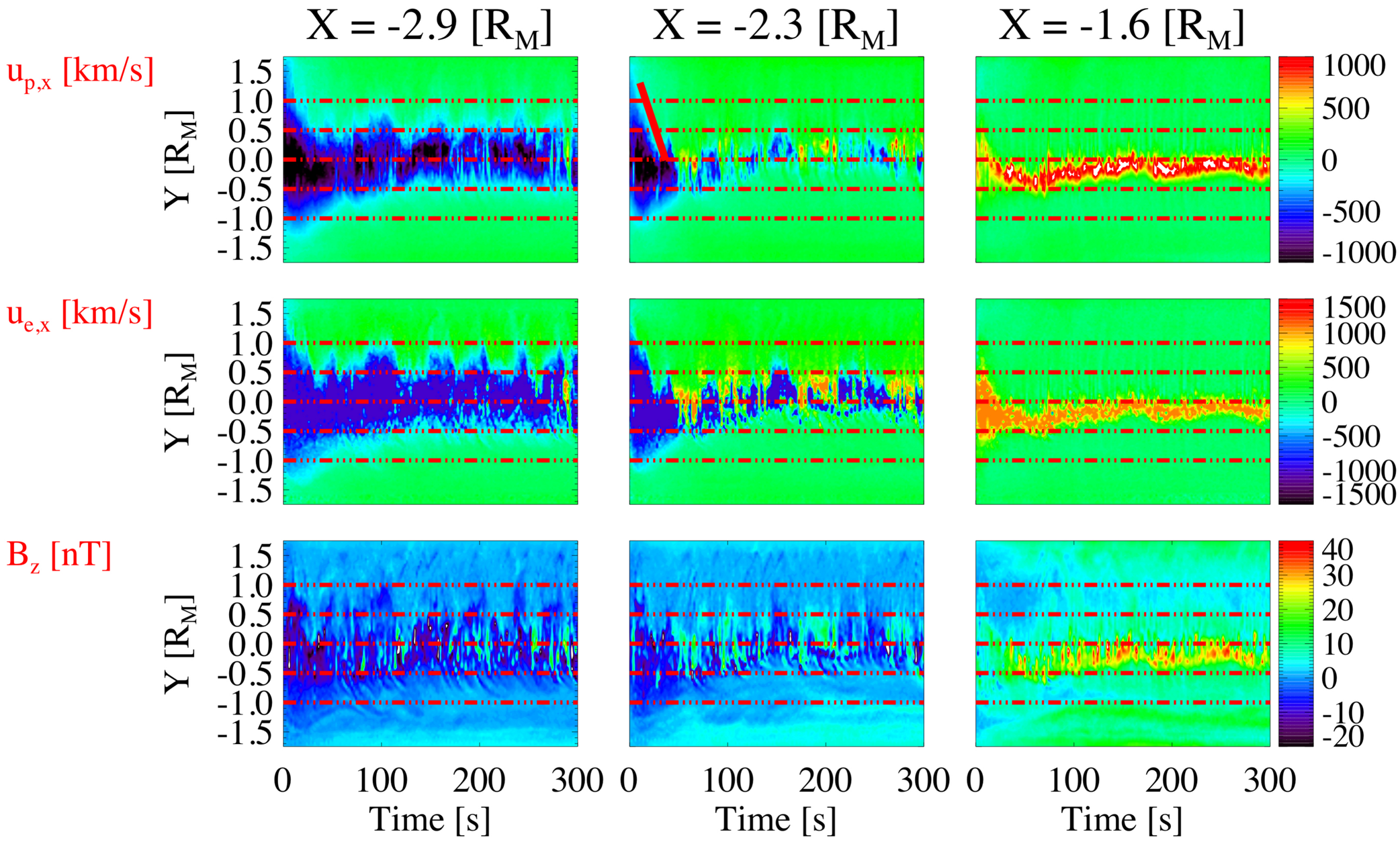

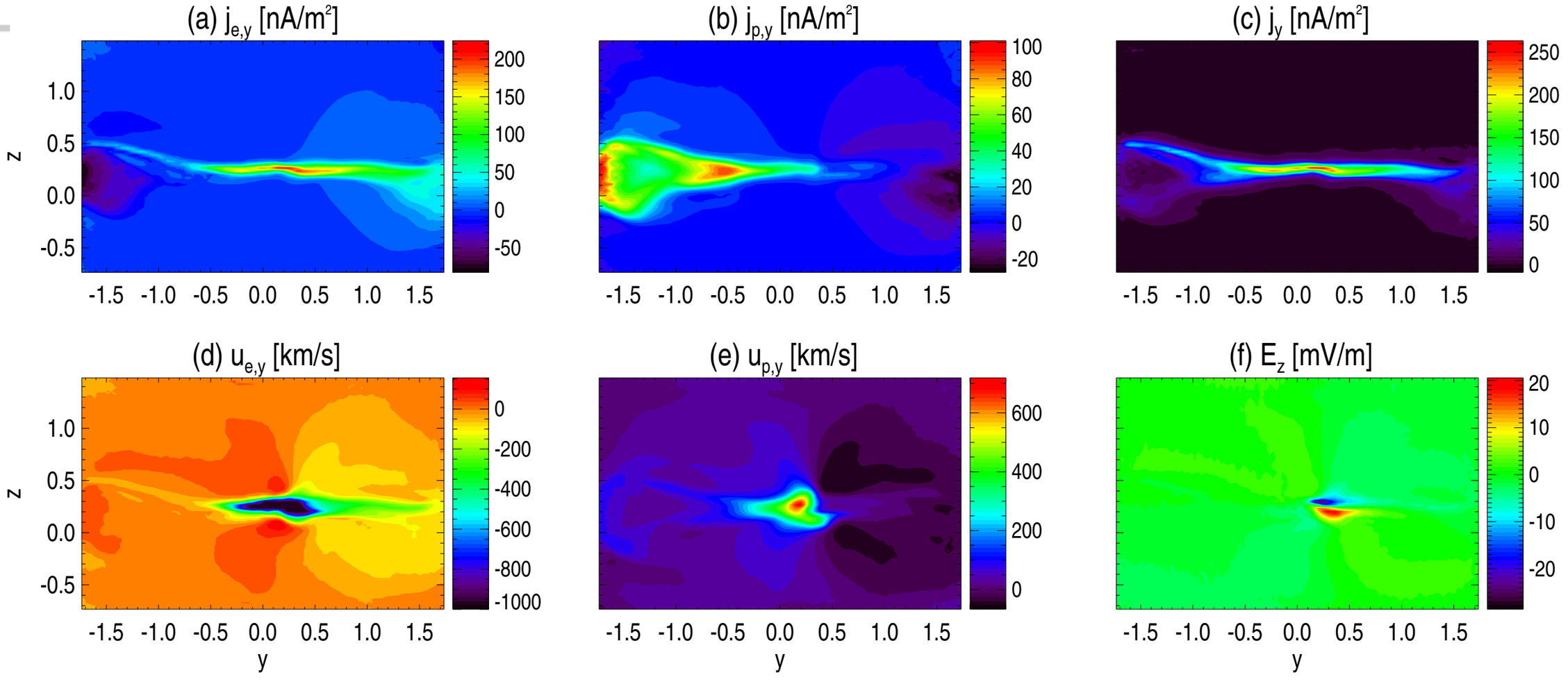

na.

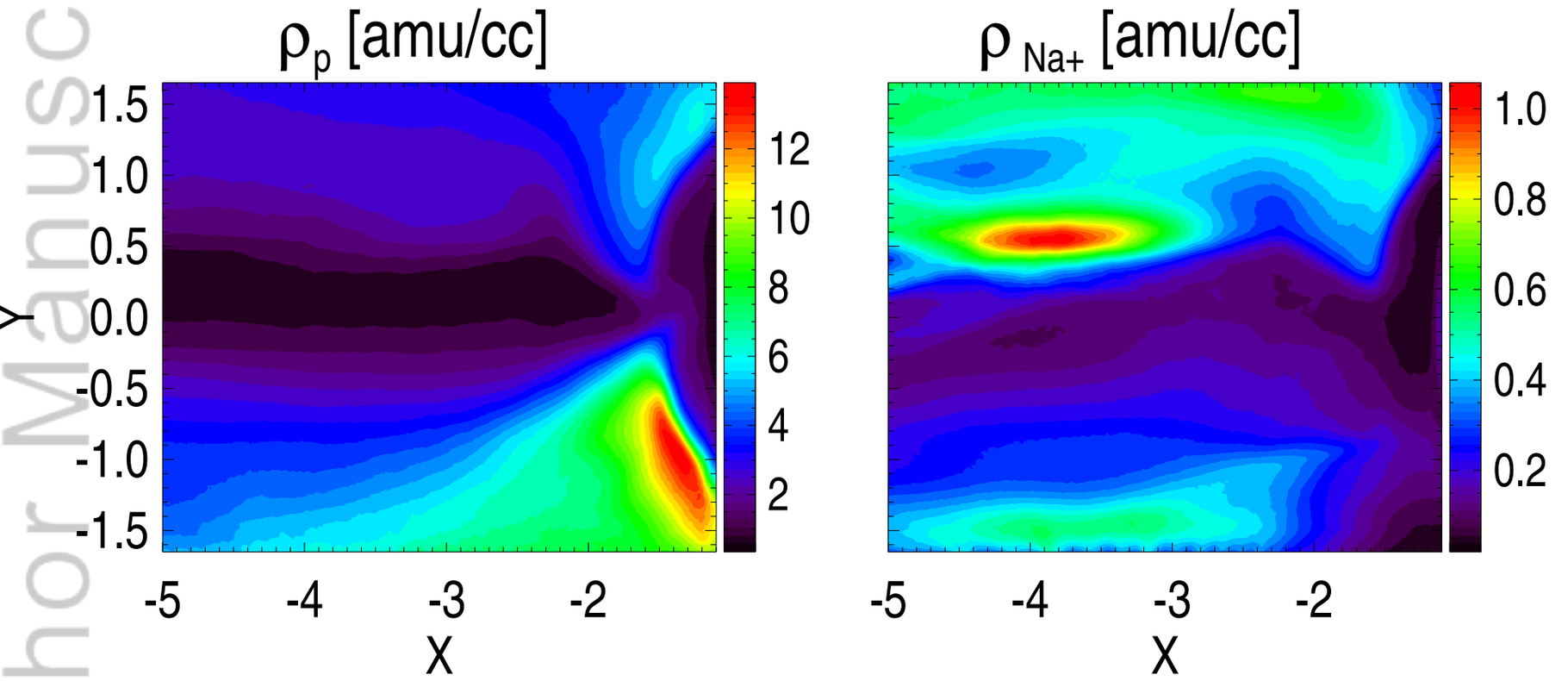

observation_df.

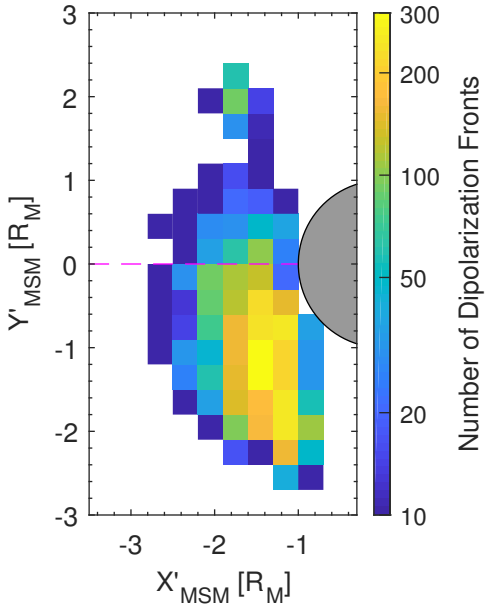

observation_plasma.

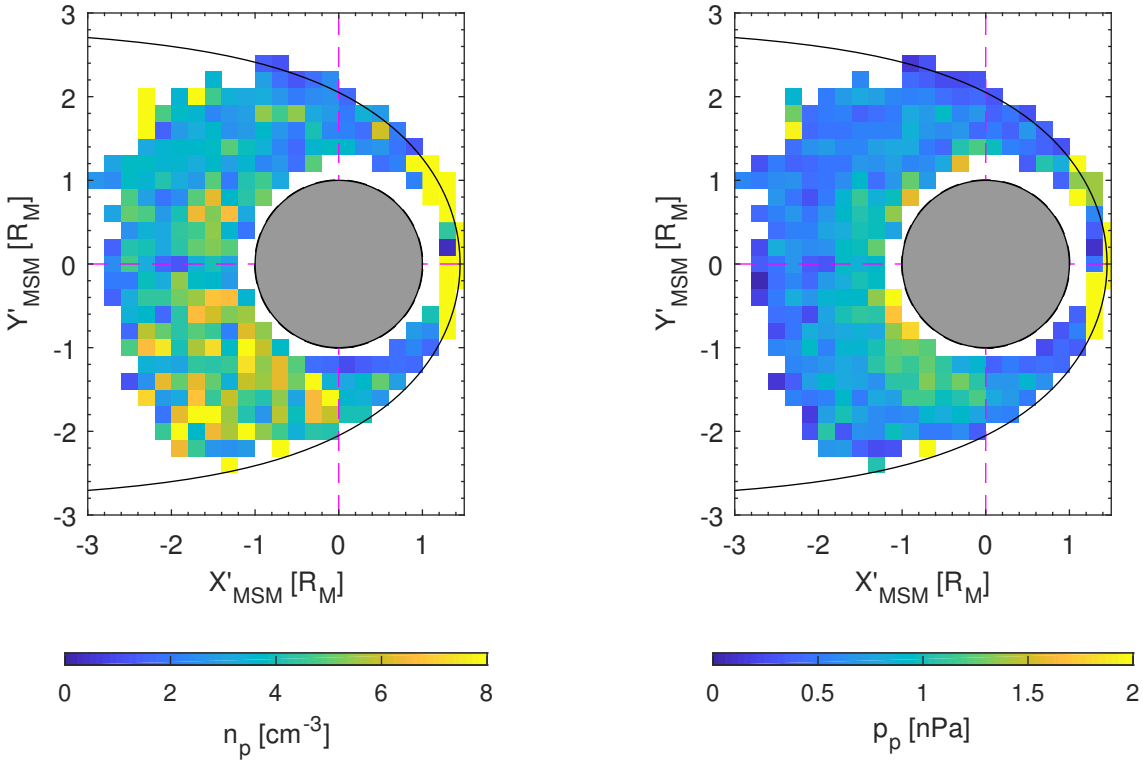

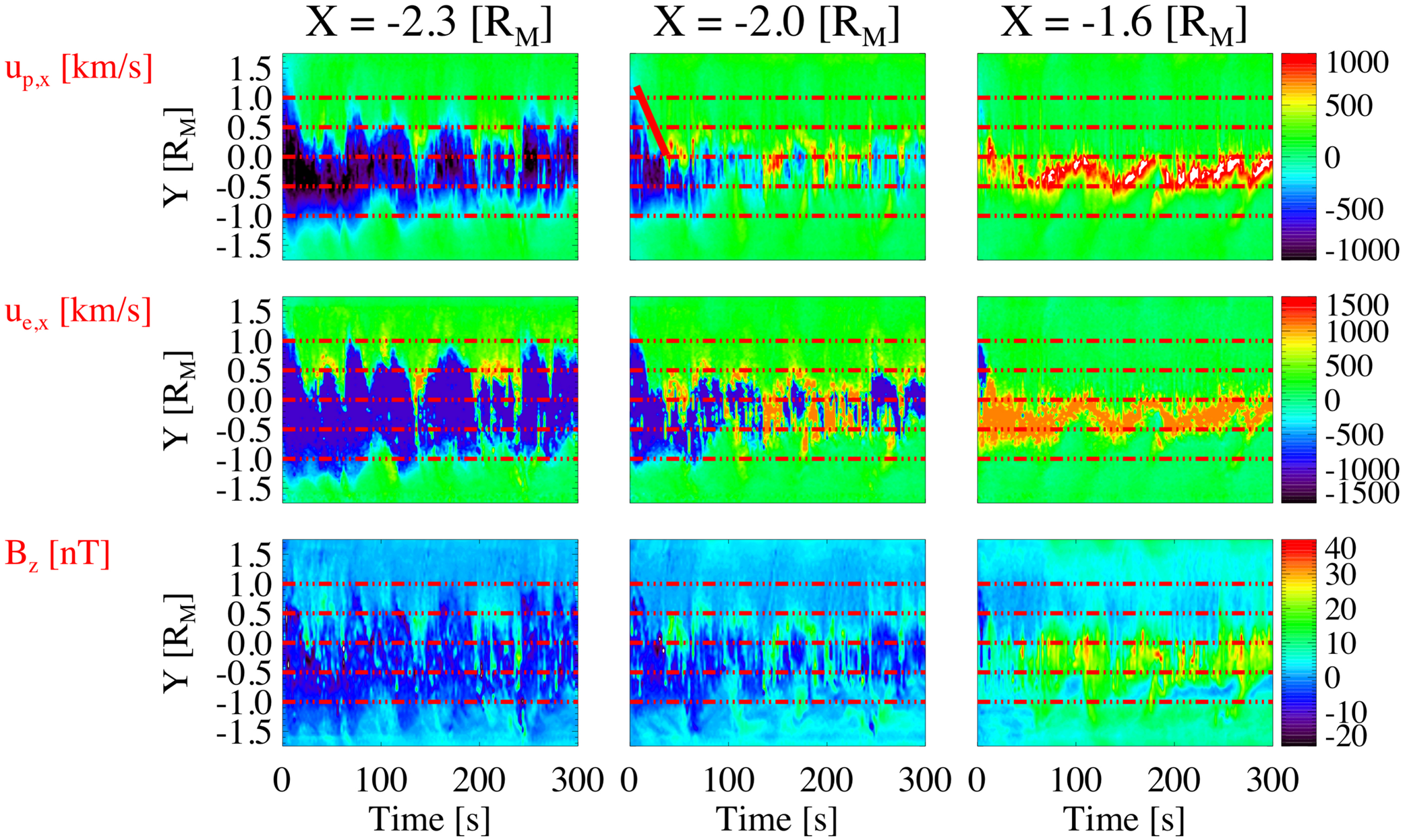

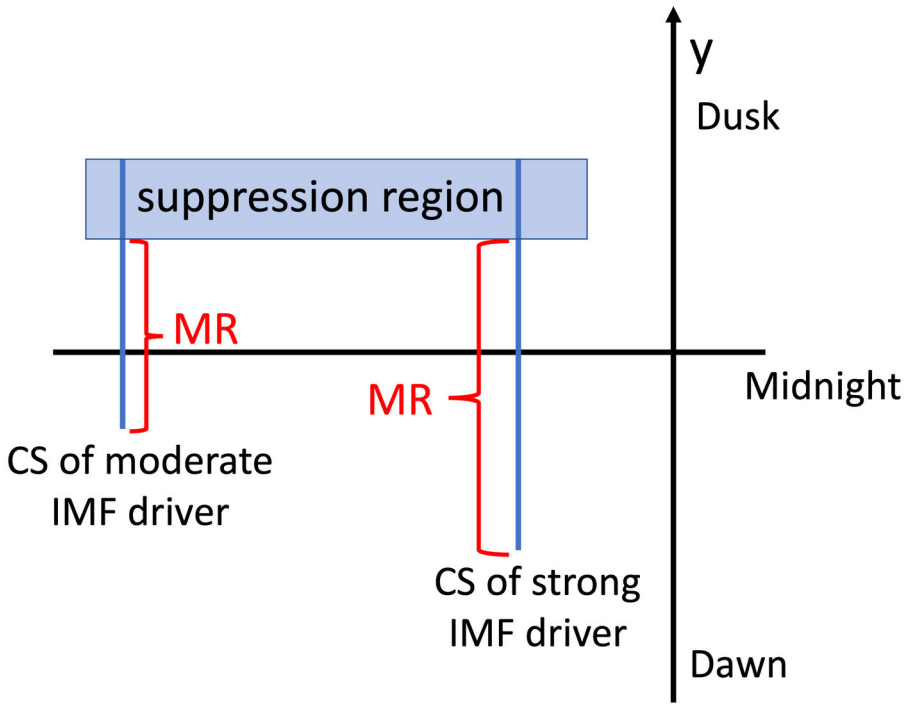

2019JA026840-f01-z-.jpg

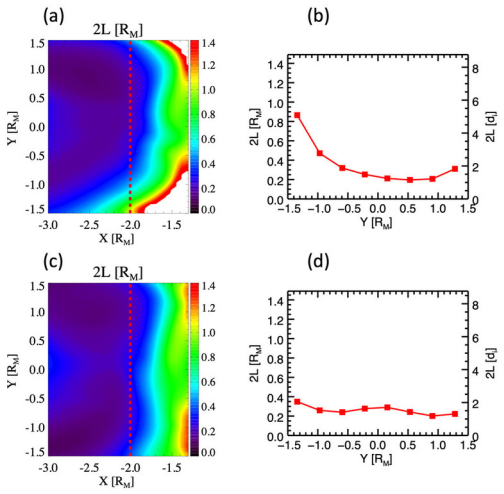

2019JA026840-f02-z-.jpg

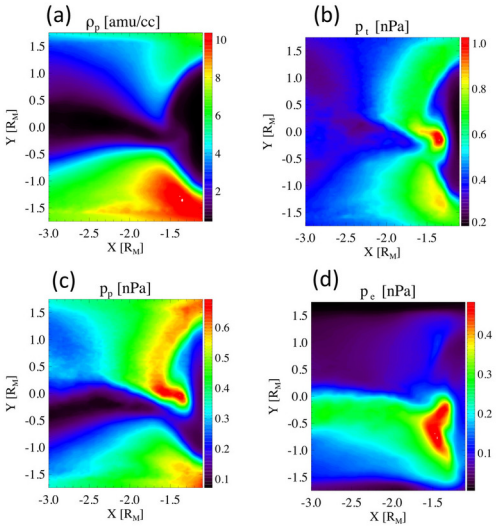

2019JA026840-f03-z-.jpg

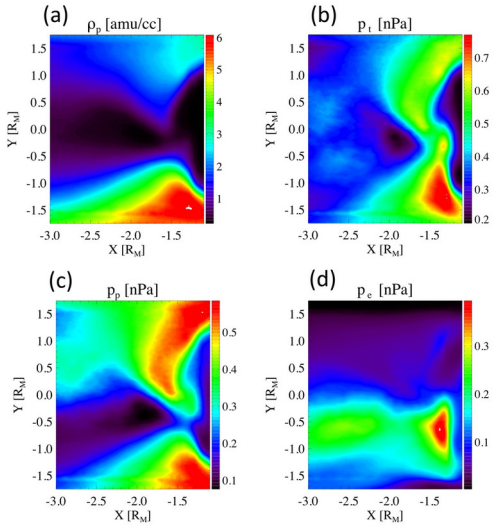

2019JA026840-f04-z-.jpg

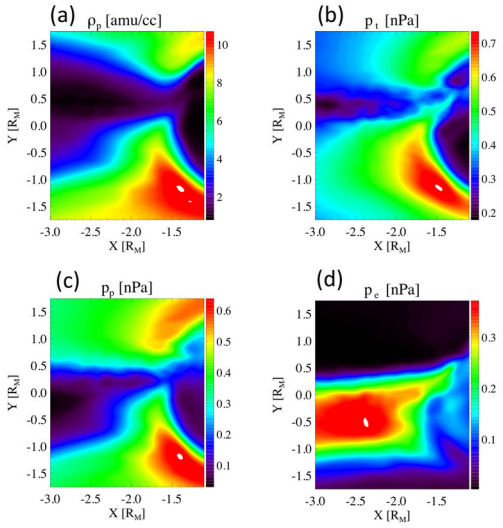

2019JA026840-f05-z-.jpg

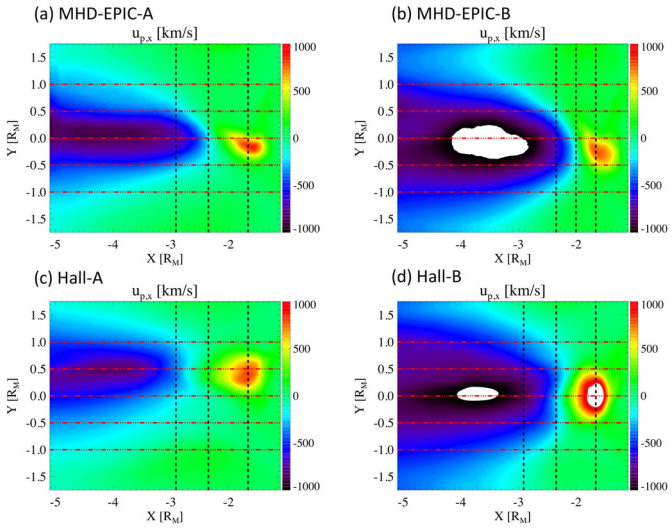

2019JA026840-f06-z-.jpg

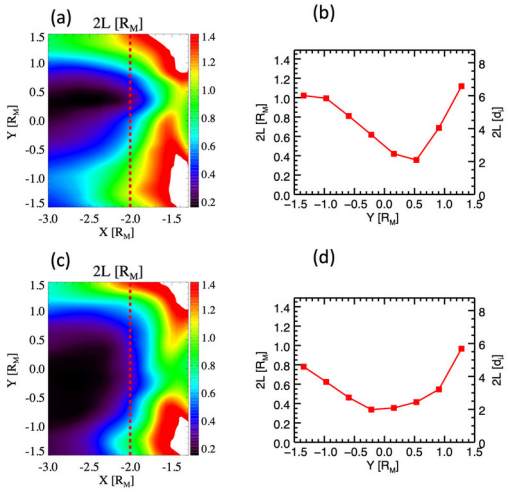

2019JA026840-f07-z-.jpg

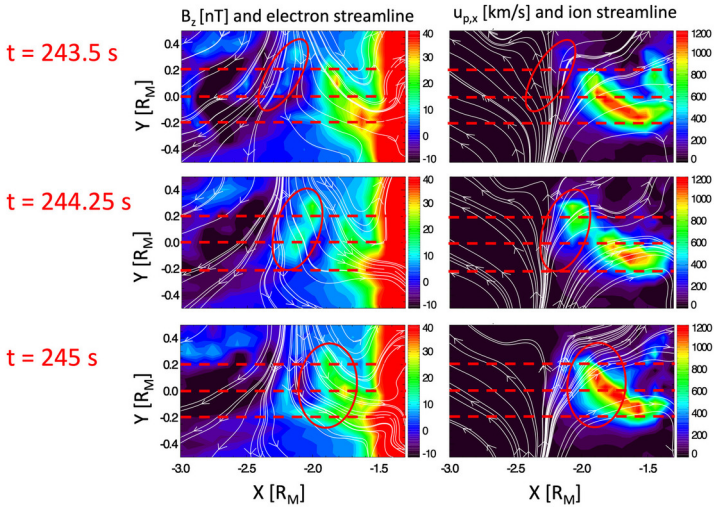

2019JA026840-f08-z-.jpg

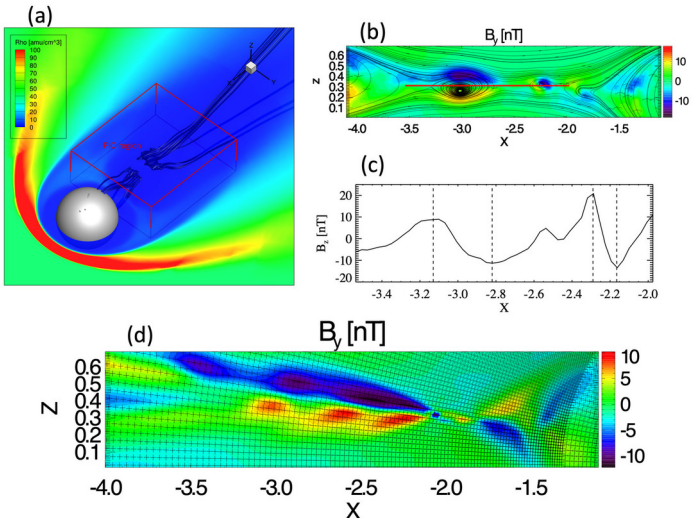

2019JA026840-f09-z-.jpg

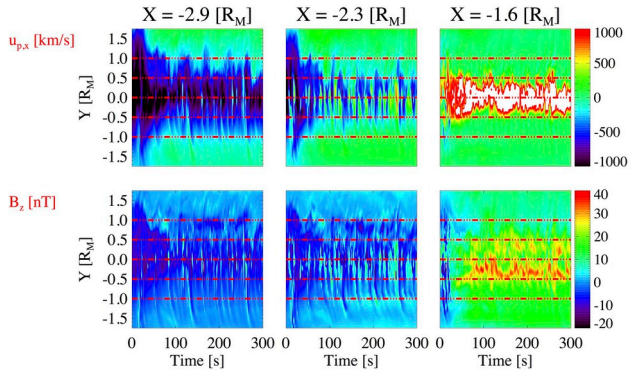

2019JA026840-f10-z-.jpg

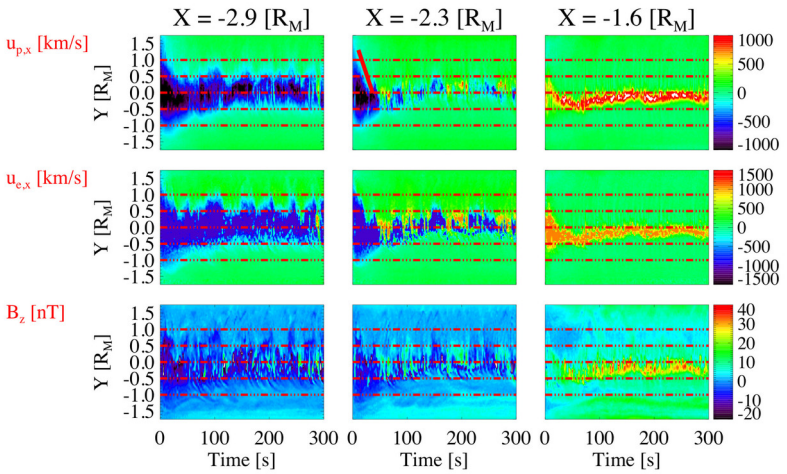

2019JA026840-f11-z-.jpg

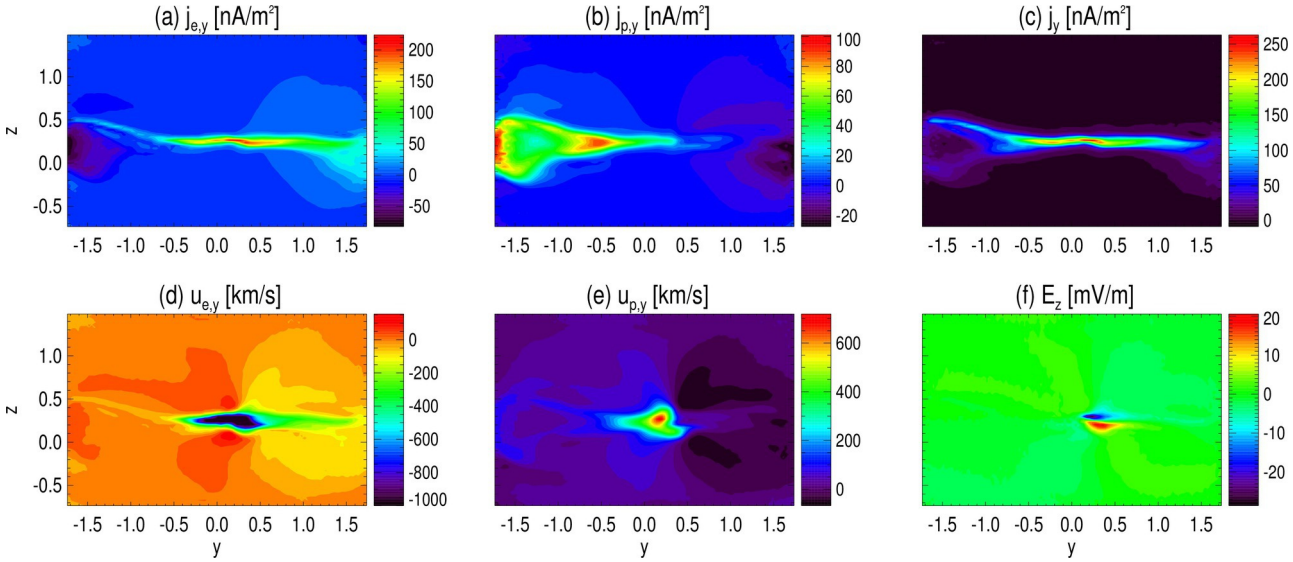

2019ja026840-f12-z-.eps

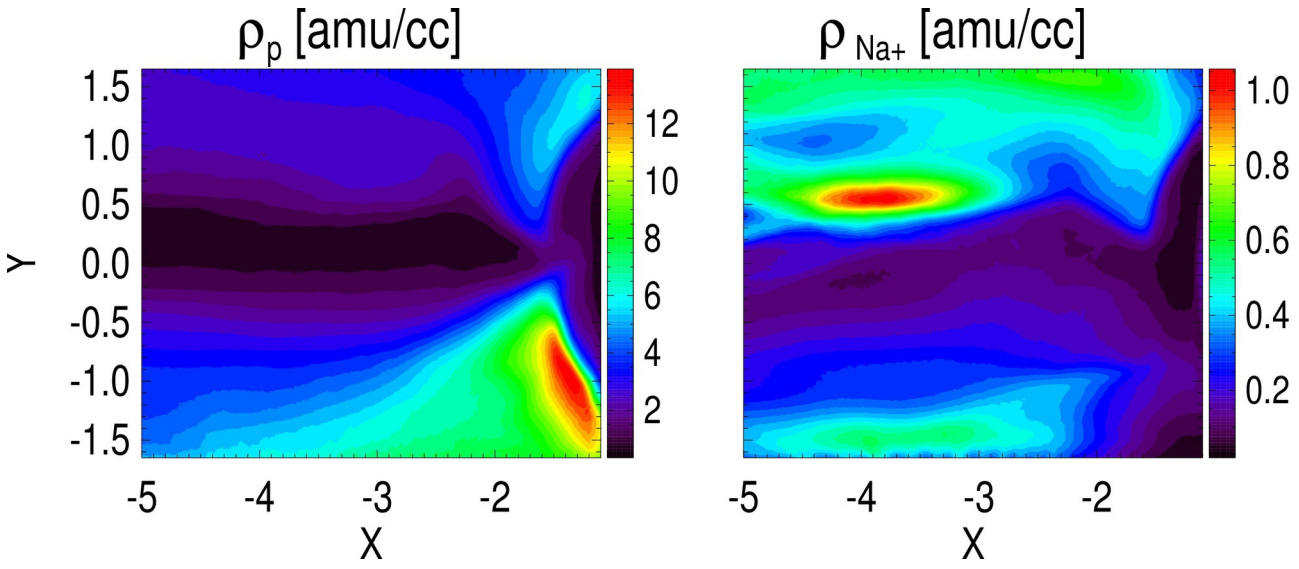

2019ja026840-f13-z-.eps

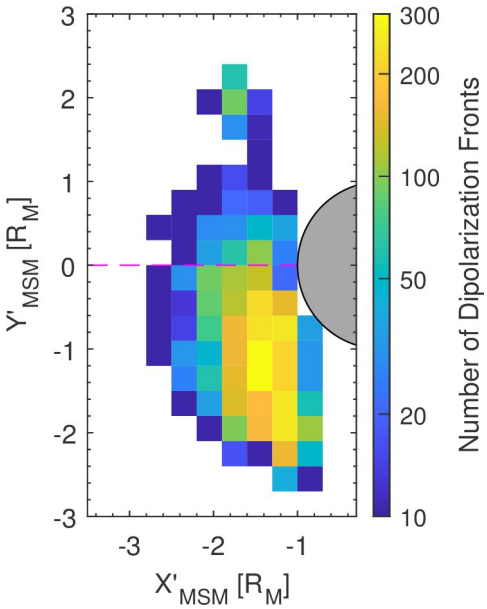

2019ja026840-f14-z-.eps

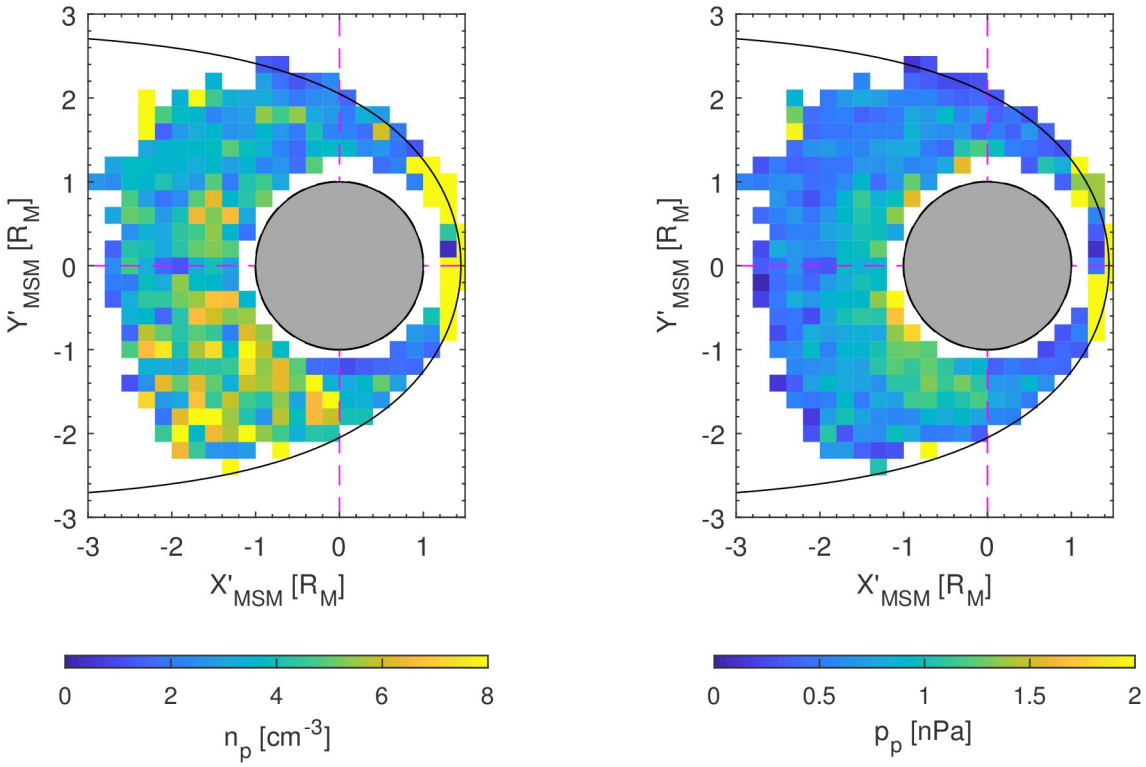

2019ja026840-f15-z-.eps

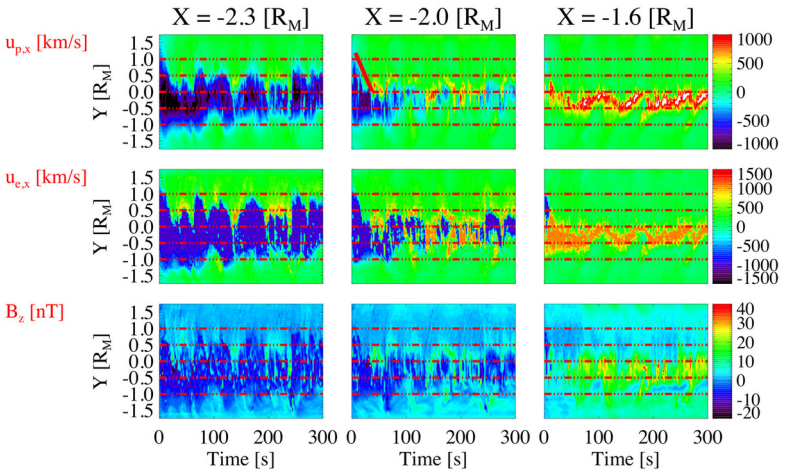

2019JA026840-f16-z-.jpg